Data-driven vibration prognosis using multiple-input finite impulse response filters and application to railway-induced vibration of timber buildings

Benedikt Hofmeister*, Stefan Wernitz, Tanja Grießmann, Clemens Hübler, Raimund Rolfes

Leibniz University Hannover, Institute of Structural Analysis, Appelstr. 9A, 30167 Hannover, Germany

Abstract

With this paper, we present a vibration prognosis method based on finite impulse responses. The impulse responses are identified using measurement data from an existing building and consider a multiple-input/multiple-output topology.

Vibration prognosis in urban buildings is becoming increasingly important, since more and more buildings are being constructed close to urban infrastructure. Combined with modern and ecological choices of building materials and the low vibration levels required by current standards, serviceability in terms of structural dynamics becomes an issue. Sources of vibration in urban settings include railway and metro lines as well as road traffic. This work focuses on a method especially suited to the three-dimensional vibration state encountered in modern timber buildings. Under the assumption of linear time-invariant structural dynamic behaviour, we develop a time-domain identification approach. The novelties of this contribution lie in the formulation of a numerically efficient method to identify multiple-input finite impulse response filters and its application to measurement data of a timber building.

We validate this data-driven prognosis method using measurement data from a building constructed from cross-laminated timber, considering the three-dimensional vibration behaviour. The accuracy and limitations are assessed using railway-induced vibrations as a typical source of disturbance by infrastructure. We show that vibration data from the foundation can be used for effective prognosis of the top floor slabs considering train types not included in the identification data set. Based on the prognosis method, a virtual sensor concept for long-term monitoring is presented.

---

*Corresponding author

Email address: b.hofmeister@isd.uni-hannover.de (Benedikt Hofmeister)

1. Introduction

With an increasing demand for housing, many new building projects are planned in the vicinity of urban centres and the associated transport infrastructure. Active railway lines as well as underground metro tunnels induce significant vibrations into the soil at these sites [1]. This dynamic excitation is transmitted through the soil into buildings, which can lead to excessive floor slab vibrations. For high-value real estate near the city centres, a high comfort level is required by the awarding authority. To ensure that structural damage and discomfort to the inhabitants do not occur, standards, such as the German DIN 4150-2 [2], provide acceptable vibration levels by means of guideline values. These values are determined from long-time experience and represent a conservative approach. The German standard VDI 2038-1 [3] provides further guidelines concerning the application of traditional methods for vibration prognosis.

In recent years, cross-laminated timber has become a viable construction material for regular urban housing [4]. This trend towards ecological materials is reflected by an increased demand for cross-laminated timber on the market [5]. However, timber construction features unique challenges with respect to vibration susceptibility. Due to the lower horizontal stiffness when compared to reinforced concrete buildings or steel skeleton structures [6], a three-dimensional vibration behaviour arises. Thus, not only vertical floor vibrations can become critical, but also horizontal movements of the whole building [7]. Additionally, the light weight of the structures leads to an increasing dynamic excitability of timber buildings compared to conventional concrete or masonry buildings. These circumstances can lead to elevated vibration levels which may become severe enough to disturb the inhabitants. Several experimental studies were thus recently conducted involving structures made from cross-laminated timber. These include a detailed modal study of a floor panel by Kawrza et al. [8] as well as the measurment of the three-dimensional dynamics of w whole building by Mugabo et al. [9].

Since standards are in place which regulate the maximum permissible vibration levels [2], liability issues can arise when limits are exceeded. Due to the variability associated with dynamic excitation sources in urban centres, accurate prognosis can be a challenging task. A vibration prognosis method suitable for the aforementioned context should therefore allow for the prognosis of previously unknown types of excitation, for example different types of trains. Additionally, the method should

yield prognosis data for the vertical and the horizontal directions and should enable a virtual sensing to extend the time frame and increase the acceptability of measurement campaigns. Further, the vibration estimation model needs to handle a wide variety of excitation scenarios, which can have both transient as well as stationary signal characteristics. Timber buildings exhibit complex three-dimensional vibration states, so the method should include data from multiple sensor positions and measurement directions at once to enable a robust and stable prognosis. Since horizontal vibration modes of the whole building as well as vertical modes of the floor slabs have to be considered, a large number of vibration modes are in the frequency range of interest, which need to be captured by the method of choice. Finally, the residents usually occupy their apartments during the measurement time frame, so signal contamination is inevitable. A common cause of signal contamination in such a setting is the vibration caused by persons walking on the floor slabs of their apartments. Hence, vibration prognosis methods need to be robust against signal contamination caused by events unrelated to the railway-induced vibration. Additionally, timber buildings are complex mechanical structures consisting of many individual parts connected by a large amount of fasteners. A finite element model-based approach would thus be very time-consuming due to the large number of engineering details which would need to be considered during modelling.

To date, much experimental experience has been gained in the field of rail traffic vibrations. For example, Tao et al. [10] published detailed vibration and noise measurements in a typical 28-story residence and a 4-story steel-framed office building during train pass-by events in a metro depot. Measured points were set at ground level adjacent to the building support structures as well as on upper floors. Transmissibiliy functions for soil-structure interactions were studied by Kouroussis et al. [11] focusing on vibrations caused by metro lines. A number of authors have researched vibration and noise prediction methods for buildings excited by train traffic based on the finite element (FE) method. Ibrahim and Nabil [12] presented a detailed FE analysis and parameter study conducted on a ten-story reinforced concrete framed structure resting on a raft foundation. Train loads are modelled using moving point sources considering varying distances between excitation source and the building as well as varying train track spacing and train speeds. To overcome the problem of computational inefficiency, Amando-Mendes et al. [13] introduced a coupled approach to model the interaction between trains, tracks, tunnels and the soil by solving the elastic 2.5D problem with the meshless Method of Fundamental Solutions (MFS) in combination with an FE approach. The latter was used to discretise the embedded structure, whereas MFS was adopted to model the

unbounded soil. As an important result, the model delivers free-field responses as possible input data for subsequent prediction models for buildings. A similar approach was proposed by Zou et al. [14]. For the analysis of complex vibro-acoustic systems, Cicirello and Langley [15] proposed a hybrid method consisting in a combination of Statistical Energy Analysis (SEA) subsystems and FE components by assuming the FE components to have fully deterministic properties, while the SEA subsystems have a high degree of randomness. The SEA subsystems ensemble is dealt with analytically, while the effect of the additional FE components ensemble was approximated using Monte Carlo simulations.

For a model-based vibration prognosis, Eftekhar et al. [16] proposed a dual Kalman filtering approach for the input and vibration estimation of a 39-story building. In their study, the Kalman filter was formulated using a reduced-order finite element model. A similar approach was followed by Maes et al. [17] for Kalman filter-based virtual strain sensing on an offshore wind turbine tower. A method which directly incorporates the mode shapes resulting from the finite element model for virtual sensor estimation is known as modal expansion [18, 19]. Further, Kullaa [20] extended the modal expansion method using a Bayesian approach to increase its robustness and verified it using a finite element model of a frame structure. While finite element-based approaches can achieve highly accurate results, both modelling and analysis of a whole building can be time consuming. Moreover, model updating strategies are required to match the dynamic behaviour of the regarded structure with the finite element model [21]. In some cases, such as for Kalman filtering, model reduction needs to be applied to enable an online processing of the simulation model. Thus, data driven approaches are preferable to avoid the labour-intensive physical modelling.

In parallel to the development of FE-based, hybrid FE-MFS or FE-SEA approaches, transfer functions in combination with simplified analytical impedance models form another research branch in the field of vibration forecast for buildings. The main advantage of analytical approaches is the high computational efficiency and a good forecasting ability, when the analytical models are validated by measurements and applied to structures with similar excitation, transmission and receiver characteristics. Sanayei et al. [22, 23] presented an analytical method to calculate the transfer properties of columns and floor slabs inside a building. In their method, the impedance of various structural parts of the building is calculated and the results are combined to obtain the transfer functions. In the work of Zou et al. [24], transfer functions for multi-story buildings were derived from analytical 1D and 2D impedance models and validated by measured railway-induced

4

vibrations at the foundation level and on upper floors in 14-story and 25-story buildings. Auersch [25] follows a similar methodology using a physically-based prediction scheme consisting of transfer matrices for the rail and the building. The soil is modelled using a homogeneous half-space with a frequency-dependent wave velocity.

In addition to methods based on physically motivated modelling, purely data-driven approaches for vibration estimations have been proposed. The main advantage of these methods is that no knowledge about the mechanical properties of the building is needed in order to apply them for vibration estimation. A data-driven approach employing multiple-input transfer functions presented by Weijtjens et al. [26] is based on solving for the spectral contributions of multiple sensors to the measured signal of another sensor. This is enabled by using a H1 or H2 estimation technique [27]. However, the frequency-domain identification is limited to cases where multiple uncorrelated excitation sources are present [28], which is not generally the case for buildings subjected to traffic-induced vibration. Tarpø et al. [29] proposed to use mode shapes identified using operational modal analysis in a modal expansion scheme. Another data-driven estimation method is described by Peeters [30], in which a state-space model is obtained using stochastic subspace identification. By coupling the estimated state-space model to a Kalman filter, vibration estimation and virtual sensing are enabled [31]. While operational modal analysis is a widely used technique in structural dynamics, it often requires additional tools like stabilisation diagrams, increasing the complexity of this strategy. The assumption of a white noise excitation as well as white noise measurement disturbance, which operational modal analysis methods share with Kalman filtering [32, 33], is often invalid for traffic-induced vibrations of buildings. Further, modal analysis techniques perform best with sufficiently long measurements and well-observed structures that exhibit modes which are well-separated in terms of their frequency [34]. From a modal analysis standpoint, the identification of high-order mode shapes of complex buildings with few sensors is therefore a vague and tedious endeavour.

In this work, in an effort towards a robust data-driven vibration prognosis method, an approach based on multiple-input finite impulse response (FIR) filters is presented. Special consideration is given to the numerical performance of the identification procedure. The basic idea for multiple-input FIR filters was presented by Powell et al. [35]. An advanced method for data-driven identification of such filters was introduced by Chen et al. [36] and is incorporated in MATLAB [37]. Filters with thousands of coefficients are required to accurately describe the vibration behaviour of the

5

building investigated in this paper. However, existing approaches such as the MATLAB function `impulseest` [37] require a prohibitive amount of computational effort for these extreme filter orders.

125   Concerning the earlier-mentioned requirements for estimation of railway-induced vibration in timber buildings, FIR filters are well suited due to their ability to accurately describe both transient and stationary vibration events over a broad frequency range [38]. The adopted multiple-input topology is able to cope with the complex three-dimensional vibration state of the building and the robust data-driven identification scheme suppresses signal contamination and disturbances. Further,

130 short-term vibration measurement data of floors of an existing building can be used to derive FIR filter models. These FIR filters can then be applied to obtain virtual sensor vibration time series using only measurement data from a small subset of sensors. In addition to its application for vibration prognosis, the FIR filter has been applied to observers in controller design [39, 40] and digital signal processing [41, 42].

135   To validate the proposed method, vibration measurement data obtained from a timber building is used. The building is situated close to train tracks and data sets of various train types were captured using vibration velocity sensors. A preliminary study to estimate the optimal filter order is conducted. Subsequently, the prognosis accuracy is evaluated using various combinations of train types and sensors.

140   Therefore, the first novelty of this work is the usage of an interpolation scheme, which allows for computing times on a manageable level for data-driven vibration prognosis. The second novelty relates to the application of this scheme to vibration prognosis of a timber building using measurement data.

    This paper is divided into three main sections: First, a derivation of a numerically efficient

145 multiple-input/multiple-output FIR identification method as well as an automated procedure for model selection is given. Second, the measurement setup and acquired data of a timber structure are presented. Finally, the results obtained using the new method and the measurement data are shown and discussed.

2. Identification of multiple-input/multiple-output impulse responses

150   In digital filter theory, FIR filters are used to model the response of linear time-invariant systems. Using these filters, a vibration time series recorded at one position of a structure can be transformed into another time series, representing the vibration time series at a different location [43]. Figure 1

6

shows a schematic figure of a building with two measurement positions x and y, which represent the measurement channels at the input and output of a prognosis filter. In this example, the vertical measurement direction is indicated by an arrow at the respective measurement positions.
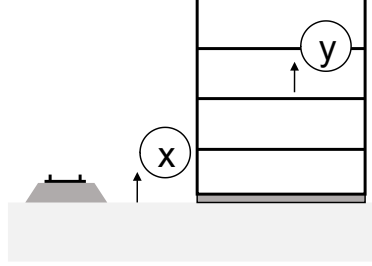

Figure 1: Schematic diagram showing a structure next to train tracks as well as soil measurement position x and floor slab measurement position y with vertical measurement directions.

The equations of motion of a damped linear mechanical system with multiple degrees of freedom can be stated as [44]

$$\boldsymbol{M}\ddot{\boldsymbol{u}}(t) + \boldsymbol{C}\dot{\boldsymbol{u}}(t) + \boldsymbol{K}\boldsymbol{u}(t) = \boldsymbol{p}(t), \tag{1}$$

where $\boldsymbol{u}(t)$ is the displacement vector associated with the degrees of freedom, $\boldsymbol{M}$ is the mass matrix, $\boldsymbol{C}$ is the damping matrix, $\boldsymbol{K}$ is the stiffness matrix and $\boldsymbol{p}(t)$ is the vector of external forces. This mechanical formulation can be transformed to the state-space representation to make it more readily tractable using control theory

$$\begin{bmatrix} \dot{\boldsymbol{u}}(t) \\ \ddot{\boldsymbol{u}}(t) \end{bmatrix} = \underbrace{\begin{bmatrix} \boldsymbol{0} & \boldsymbol{I} \\ -\boldsymbol{M}^{-1}\boldsymbol{K} & -\boldsymbol{M}^{-1}\boldsymbol{C} \end{bmatrix}}_{\boldsymbol{A}_u} \begin{bmatrix} \boldsymbol{u}(t) \\ \dot{\boldsymbol{u}}(t) \end{bmatrix} + \underbrace{\begin{bmatrix} \boldsymbol{0} \\ \boldsymbol{M}^{-1} \end{bmatrix}}_{\boldsymbol{B}_u} \boldsymbol{p}(t) \tag{2a}$$

$$\boldsymbol{v}(t) = \underbrace{\begin{bmatrix} \boldsymbol{0} & \boldsymbol{I} \end{bmatrix}}_{\boldsymbol{C}_u} \begin{bmatrix} \boldsymbol{u}(t) \\ \dot{\boldsymbol{u}}(t) \end{bmatrix} + \underbrace{\begin{bmatrix} \boldsymbol{0} \end{bmatrix}}_{\boldsymbol{D}_u} \boldsymbol{p}(t). \tag{2b}$$

Equation 2a is the state equation which is equivalent to Equation 1. Equation 2b is the output equation, which is used to extract the vibration velocities $\boldsymbol{v}(t)$ from the state vector in this case. The matrices $\boldsymbol{A}_u$, $\boldsymbol{B}_u$, $\boldsymbol{C}_u$ and $\boldsymbol{D}_u$ can be further employed to find the impulse response of the mechanical system. One can show that for a steady state, the velocities can also be expressed as

7

[45]

$$\boldsymbol{v}(t) = \int_{t_0}^{t} \boldsymbol{G}(t - \tau)\boldsymbol{p}(\tau)\mathrm{d}\tau \tag{3a}$$

$$\boldsymbol{G}(t) = \boldsymbol{C}_u e^{\boldsymbol{A}_u t}\boldsymbol{B}_u, \tag{3b}$$

where $\boldsymbol{G}(t)$ is the matrix of impulse response functions. The impulse responses can be obtained using the Equation 3b. Using the convolution integral shown in Equation 3a, the dynamic response of the mechanical system can be modelled solely the impulse response and the external forces. Since the external forces are often unknown in structural dynamics, vibration data acquired using sensors affixed to the structure can be used as a proxy. A vibration prognosis of position y can thus be carried out by feeding vibration data recorded at position x into an appropriately identified FIR filter. This filter structure can also be expressed by the system model

$$x \longrightarrow \boxed{\boldsymbol{b}} \longrightarrow \hat{y} \; ,$$

where the filter coefficients $\boldsymbol{b}$ represent the transfer function from the input to the output. Throughout this paper, the 'hat' notation indicates that $\hat{y}$ is an estimated value as opposed to y which represents measured data at the output.

The mathematical definition of the FIR filter resembles the discrete convolution [38]

$$\hat{y}[i] = \sum_{j=0}^{M} b[j] \; x[i - j], \tag{4}$$

where input and output time series are represented by the vectors $\boldsymbol{x}$ and $\hat{\boldsymbol{y}}$, respectively. Equation 4 therefore resembles the single-input/single-output discrete formulation analogous to Equation 3a. The parameter M represents the filter order and the vector $\boldsymbol{b}$ therefore consists of $M + 1$ filter coefficients where j represents an index to this vector. The index i denotes a sample in the output time series $\hat{\boldsymbol{y}}$ as well as an offset in the input time series $\boldsymbol{x}$. With the formulation according to Equation 4, we imply causality of the filter, which means that changes at the output $\hat{y}$ must not temporally precede changes in the input x.

2.1. Single-input finite impulse response identification

A FIR filter is identified by finding a vector of filter coefficients $\boldsymbol{b}$, which transforms the input signal x, so that it approximates the measured output signal y as good as possible. This means that

8

the residual signal power between the filter response $\hat{y}$ and the measured output y signal has to be minimised. Filter identification also requires that the time series x and y have to be recorded using a fixed sampling rate and be synchronised to prevent temporal drift over time. The unconstrained linear least squares optimisation problem yielding $\boldsymbol{b}$ can be expressed as [43]

$$\underset{\boldsymbol{b}}{\text{minimise}} \sum_{i=M+1}^{m} \left(y[i] - \sum_{j=0}^{M} b[j]\, x[i-j] \right)^2 , \tag{5}$$

where m denotes the number of samples in the time series $\boldsymbol{x}$ and $\boldsymbol{y}$. In order to make this problem tractable using linear algebra, Equation 4 is rewritten using a matrix-vector multiplication [43]

$$\boldsymbol{T} \cdot \boldsymbol{b} = \hat{\boldsymbol{y}}, \tag{6}$$

where $\boldsymbol{T}$ is a $(m-M-1) \times (M+1)$ Toeplitz matrix containing data from m measurement samples. The matrix contains the samples of the filter input $x[i]$ shifted to the respective temporal positions to result in a FIR filter, so that

$$T_{ij} = x[i-j]. \tag{7}$$

Equation 6 assumes the form of an over-determined system of equations, when the number of samples m is larger than the order of the FIR M. To attenuate the influence of measurement noise and signal contamination, it is beneficial to derive the coefficients $\boldsymbol{b}$ with $m \gg M$, so that an average solution is achieved.

Using the Moore-Penrose pseudoinverse, a least-squares optimal solution to Equation 5 is obtained, which is known as the Affine Projection Algorithm [46]

$$\boldsymbol{b} = \left(\boldsymbol{T}^{\mathsf{T}} \boldsymbol{T} \right)^{-1} \boldsymbol{T}^{\mathsf{T}} \boldsymbol{y}. \tag{8}$$

Equation 8 however does usually not yield a usable filter in practice, since measurement noise can deteriorate the quality of the identification. This can be mitigated in part by providing large amounts of measurement data from diverse excitation states. However, the high-frequency response usually contains artefacts caused by overfitting, since the signal-to-noise ratio worsens in the high-frequency domain for measurements of buildings.

The effects of overfitting can be reduced by employing the Tikhonov regularisation [47], which results in a regularised form of the Affine Projection Algorithm [48]

9

$$\boldsymbol{b} = \left(\boldsymbol{T}^{\mathsf{T}}\boldsymbol{T} + \lambda\boldsymbol{I}\right)^{-1}\boldsymbol{T}^{\mathsf{T}}\boldsymbol{y}, \tag{9}$$

where λ is a regularisation parameter and $\boldsymbol{I}$ is the identity matrix. Low values of λ lead to solutions close to those obtained without any regularisation applied. High values lead to very smooth spectra, while underestimating the vibration level significantly. An automated procedure for determining the numerical value of the regularisation parameter is discussed in Section 2.4.

The smoothing effect of the regularisation parameter λ depends on the filter order and the amplitude of the input signal. Hence, we propose a normalised formulation

$$\lambda = \lambda_0 \, \frac{\left\|\boldsymbol{T}^{\mathsf{T}}\boldsymbol{T}\right\|_{\mathrm{F}}}{M + 1}, \tag{10}$$

where $||\cdot||_{\mathrm{F}}$ indicates the Frobenius norm and $\lambda_0 \in \mathbb{R}^+$ is the normalised regularisation parameter. The Frobenius norm is linked to the energy of the input signal, hence λ becomes proportional to the signal amplitude according to Equation 10. The Frobenius norm is defined as

$$\|\boldsymbol{A}\|_F := \sqrt{\sum_i \sum_j |A_{ij}|^2}, \tag{11}$$

where A_{ij} are the elements of a matrix $\boldsymbol{A}$.

The smoothing is thus invariant to the number of samples considered in the Toeplitz matrix $\boldsymbol{T}$. To eliminate the dependency on the filter order as well, Equation 10 includes a division by $M + 1$.

2.2. Expansion to multiple-input/multiple-output identification

The motion of buildings excited by environmental vibrations is inherently three-dimensional. When a train passes close to a building, the soil, foundations and building floors vibrate in both horizontal and vertical directions. These spacial motions can be captured using triaxial sensors, as schematically illustrated in Figure 2. An uncoupling of movements in different directions is only possible for simple mechanical structures. In residential buildings, the motions are coupled in complex ways, which depend on the modal parameters as well as on the wave propagation properties of the structure. To efficiently utilise the information contained in the recorded signals, the filter identification method is thus extended to account for coupling effects from all spacial directions.

A multiple-input concept for estimation of multiple-input/multiple-output FIR filters was presented by Chen et al. [36]. The transfer characteristics can be expressed as
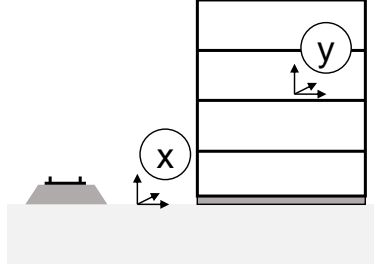
10

Figure 2: Schematic diagram showing triaxial vibration measurement positions in the soil and on a floor slab. Triaxial sensors x and y used as the input and output, respectively.

$$\begin{pmatrix} x_1 \\ x_2 \\ x_3 \end{pmatrix} \longrightarrow \begin{bmatrix} \boldsymbol{b}_{11} & \boldsymbol{b}_{12} & \boldsymbol{b}_{13} \\ \boldsymbol{b}_{21} & \boldsymbol{b}_{22} & \boldsymbol{b}_{23} \\ \boldsymbol{b}_{31} & \boldsymbol{b}_{32} & \boldsymbol{b}_{33} \end{bmatrix} \longrightarrow \begin{pmatrix} \hat{y}_1 \\ \hat{y}_2 \\ \hat{y}_3 \end{pmatrix},$$

where we consider the 1, 2 and 3 measurement directions of triaxial sensors. The filter coefficient matrix is generally unsymmetrical, thus identifications have to be carried out individually for each filter in the matrix. For the sake of convenience, we assume a triaxial case in this derivation, however, the formulation can be readily extended to account for any number of input and output channels. For example, measurement data from two triaxial sensors could be used as the inputs $x_{1...6}$, and data from only one triaxial sensor could be used as the outputs $y_{1...3}$.

Similar to Equation 6, there is also an equivalent matrix expression that is conducive to the solution by a pseudoinverse

$$\boldsymbol{T} \cdot \boldsymbol{b} = \begin{bmatrix} \boldsymbol{T}_1 & \boldsymbol{T}_2 & \boldsymbol{T}_3 \end{bmatrix} \cdot \begin{bmatrix} \boldsymbol{b}_{11} & \boldsymbol{b}_{12} & \boldsymbol{b}_{13} \\ \boldsymbol{b}_{21} & \boldsymbol{b}_{22} & \boldsymbol{b}_{23} \\ \boldsymbol{b}_{31} & \boldsymbol{b}_{32} & \boldsymbol{b}_{33} \end{bmatrix} = \hat{\boldsymbol{Y}}, \tag{12}$$

where $\boldsymbol{T}_1$ denotes the shift matrix associated with the first input channel, $\boldsymbol{T}_2$ denotes the second channel and so forth. The time series of the outputs are denoted using the matrix $\hat{\boldsymbol{Y}}$, which has a size of $(m - M - 1) \times n_y$, where n_y denotes the number of output channels. The coefficients of the impulse responses $\boldsymbol{b}_{11}$ through $\boldsymbol{b}_{33}$ can therefore be determined simultaneously, as shown in the single-input case. In the case of one triaxial input and one triaxial output, the filter coefficients are obtained using

11

$$\begin{bmatrix} \boldsymbol{b}_{11} & \boldsymbol{b}_{12} & \boldsymbol{b}_{13} \\ \boldsymbol{b}_{21} & \boldsymbol{b}_{22} & \boldsymbol{b}_{23} \\ \boldsymbol{b}_{31} & \boldsymbol{b}_{32} & \boldsymbol{b}_{33} \end{bmatrix} = \left(\begin{bmatrix} \boldsymbol{T}_1^\mathsf{T} \\ \boldsymbol{T}_2^\mathsf{T} \\ \boldsymbol{T}_3^\mathsf{T} \end{bmatrix} \cdot \begin{bmatrix} \boldsymbol{T}_1 & \boldsymbol{T}_2 & \boldsymbol{T}_3 \end{bmatrix} + \lambda \boldsymbol{I} \right)^{-1} \cdot \begin{bmatrix} \boldsymbol{T}_1^\mathsf{T} \\ \boldsymbol{T}_2^\mathsf{T} \\ \boldsymbol{T}_3^\mathsf{T} \end{bmatrix} \cdot \boldsymbol{Y}. \tag{13}$$

The normalised regularisation parameter λ_0 as defined in Equation 10 also applies to the multiple-input case. Since the matrix $\boldsymbol{T}$ has more elements in the multiple-input case compared to the single-input case, the numerical value of its matrix norm increases. Consequently, the value of the regularisation parameter λ according to Equation 10 increases and thus, the smoothing effect of the regularisation remains constant. Equation 13 can be used to identify FIR filter for dynamically loaded structures with arbitrary excitation sources. As alluded to in Section 1, an identification of multiple-input filters in the frequency domain, as presented by Weijtjens et al. [26], can not be achieved unconditionally [28].

In the following sections, the equations are derived without loss of generality using the single-input/single-output system to simplify the notation.

2.3. Interpolated finite impulse response filters

It is possible to solve Equation 13 efficiently by exploiting the Toeplitz structure of the matrix $\boldsymbol{T}$ to evaluate the expression $\boldsymbol{T}^\mathsf{T}\boldsymbol{T}$. However, the computer memory required to store the square matrix $\boldsymbol{T}^\mathsf{T}\boldsymbol{T}$ is in many cases prohibitively large. Therefore, the numerical filter identification can be further improved by considering a filter topology with less coefficients. Sparse finite impulse response filters, also known as 'tap delay' filters [38], can significantly reduce the numerical complexity of FIR filters while maintaining a high fidelity. Instead of identifying $M + 1$ filter coefficients for the full model order, a smaller number of $N + 1$ coefficients is used. The non-zero coefficients are referred to as filter 'taps' while the remaining coefficients are usually set to zero.

The achievable sparsity depends on the high frequency damping of the system, where strongly damped systems are conducive to high reduction ratios. For band-stop filter design, a reduction of non-zero coefficients exceeding 50% can be achieved in practice [49].

To achieve the best possible sparse filter quality, it is advisable to place the filter taps where the amplitude of the dense filter coefficients is highest. Generally, in mechanical systems with viscous damping, high frequency components decay faster than low frequency components. This means that most of the energy and high-frequency oscillation is contained in the beginning of the impulse response. The filter taps should thus be placed densely at the beginning of the impulse response,

12

in order to be able to capture the high frequency content. The taps in the tail of the filter should be placed at larger distances, since low-frequency signals dominate in this section [49]. For this purpose, we propose a quadratic function to place the filter taps

$$t_k = k + (M - N)\left(\frac{k-1}{N}\right)^2, \tag{14}$$

where $k \in [1, 2, ..., N+1]$ denotes the filter tap index and t_k is the corresponding tap position. The tap position for the index $k = N + 1$ coincides with the filter coefficient $M + 1$, placing the last tap at the end of the filter.

The tap positions t_k resulting from Equation 14 are real-valued. For a direct application of sparse filters, they would have to be rounded to the next integer. However, the direct application of sparse filters leads to a poor spectral signal quality. This can be overcome by employing interpolated finite impulse response filters (IFIR) [50]. IFIR filters are based on interpolation functions, which are assigned to each filter tap. Thereby, a bandwidth limitation is achieved which improves the spectral quality. The weighting coefficients resulting from the interpolation functions are combined in the interpolation matrix $\boldsymbol{H}$, which has the size $M \times N$. By applying the matrix $\boldsymbol{H}$ to the sparse filter coefficients $\tilde{\boldsymbol{b}}$, the dense filter coefficients are recovered

$$\boldsymbol{b} = \boldsymbol{H}\tilde{\boldsymbol{b}}. \tag{15}$$

We further constrain the interpolation coefficients to have a unit sum for each sparse coefficient k

$$\sum_{j=-\infty}^{\infty} H_{jk} \overset{!}{=} 1. \tag{16}$$

This leads to a normalisation of the signal content in each of the sparse coefficients. The filter coefficients $\boldsymbol{b}$ are only defined in the interval $[0, M]$, but the interpolation functions may extend beyond this interval. The sum in Equation 16 is thus defined over the interval $[-\infty, \infty]$ to achieve a consistent formulation.

The expression in Equation 6 can be rewritten using Equation 15

$$\boldsymbol{Tb} = \boldsymbol{TH}\tilde{\boldsymbol{b}} = \boldsymbol{y}, \tag{17}$$

again representing an overdetermined system of equations. The order of multiplications in Equation 17 is modified

$$\tilde{\boldsymbol{T}} = \boldsymbol{T}\boldsymbol{H} \implies \tilde{T}_{ik} = \sum_{j=0}^{M} H_{jk}\ x[i-j], \tag{18}$$

where the shift matrix $\boldsymbol{T}$ is eliminated and replaced by a convolution of the input x with the interpolation matrix $\boldsymbol{H}$ to yield the sparse shift matrix $\tilde{\boldsymbol{T}}$. A similar scheme was put forward for adaptive IFIR filters by Wu et al. [51]. By substituting $\boldsymbol{T}$ for $\tilde{\boldsymbol{T}}$ and $\boldsymbol{b}$ for $\tilde{\boldsymbol{b}}$, Equation 9 can be rewritten to yield the sparse filter coefficients

$$\tilde{\boldsymbol{b}} = \left(\tilde{\boldsymbol{T}}^{\mathsf{T}} \tilde{\boldsymbol{T}} + \lambda \boldsymbol{I} \right)^{-1} \tilde{\boldsymbol{T}}^{\mathsf{T}} \boldsymbol{y}. \tag{19}$$

The normalised regularisation parameter λ_0 also applies for interpolated filters, since the signal energy content in $\boldsymbol{T}$ and $\tilde{\boldsymbol{T}}$ is roughly the same. This is the case, since the constraint in Equation 16 forces the interpolation filters to have a unit gain in the passband.

The choice of the interpolation functions influences the achievable quality of the identification. While triangular interpolation functions, also known as Bartlett windows, are often used for computational resource efficiency in real-time processing [52], we propose employing Gaussian functions. The latter allow for smoother interpolations than Bartlett windows in exchange for slightly higher computing times.

The centres of the Gaussian windows μ_k are placed at the real-valued tap positions, such that $\mu_k = t_k$. We propose a parametrisation of the window using

$$\sigma_k = \frac{t_{k+1} - t_{k-1}}{4}, \tag{20}$$

where σ_k is the standard deviation of the Gaussian interpolation function associated with the k-th filter tap positioned at t_k. This way, neighbouring tap positions $t_{k\pm1}$ have a distance of approximately two standard deviations. Since the area under the curve of a Gaussian distribution is always one, the constraint given in Equation 16 is readily fulfilled. An illustration of the interpolation matrix $\boldsymbol{H}$ is shown in Figure 3. The figure depicts the overlap resulting from the parameterisation given in Equation 20. The shape of a single interpolation function taken from the matrix $\boldsymbol{H}$ is shown in Figure 4 .

A benefit of Gaussian window functions is the theoretically infinite side lobe suppression in the frequency domain [53]. The frequency response of the interpolation function displayed in Figure 4 is indicated in Figure 5, where the flat section of the graph indicated for the Gaussian window close to $-250\,\mathrm{dB}$ is caused by numerical round-off error. To reduce the number of non-zero elements in
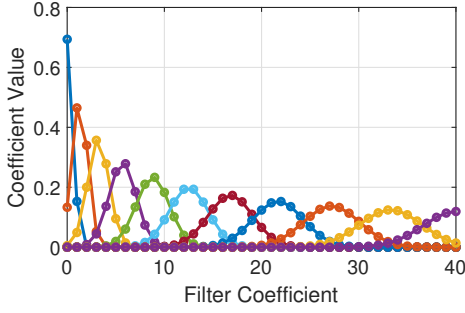
14

Figure 3: Matrix of interpolation coefficients with $N = 10$ and $M = 40$. Individual interpolation functions are each highlighted with a different colour.
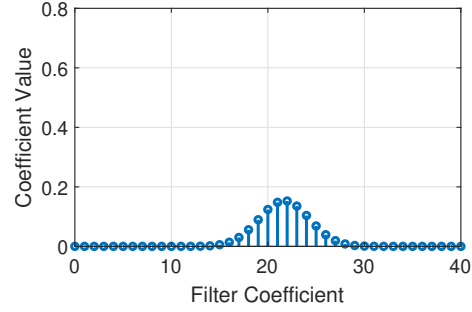

Figure 4: Interpolation coefficients of a single interpolation function shown using a stem plot.

the interpolation matrix $\boldsymbol{H}$ and thus minimise the number of multiplications required to compute the sparse shift matrix (Equation 18), we propose a truncation of the Gaussian functions. This truncation is carried out by setting the interpolation matrix coefficients H_{jk} with values below 10^{-5} to zero, which results in a side lobe suppression greater than $-100\,\text{dB}$. The spectrum resulting from truncation is superimposed in Figure 5.
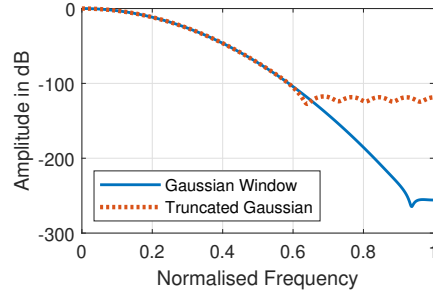
Figure 5: Frequency response spectrum for the Gaussian interpolation function shown in Figure 4. A truncation of the interpolation function leads to the emergence of side lobes.

2.4. Filter order selection

This section introduces a procedure to automatically determine the three parameters, which govern the process of filter identification. The first parameter M relates to the filter order which determines how many coefficients comprise the finite impulse response. The second parameter N relates to the number of taps of the sparse filter and thus dictates the accuracy of the sparse

15

approximation. Finally, the normalised regularisation parameter λ_0 controls how much smoothing is applied to the filter coefficients.

The statistical methods employed to select appropriate parameters are based on the estimation error of the identified multiple-input/multiple-output filter model. The error between estimated data $\hat{\boldsymbol{Y}}(M, N, \lambda_0)$ and measured data $\boldsymbol{Y}$ is expressed using the mean squared error (MSE) [54]

$$\text{MSE} = \frac{1}{m} \left(\hat{\boldsymbol{Y}}(M, N, \lambda_0) - \boldsymbol{Y} \right)^{\mathsf{T}} \cdot \left(\hat{\boldsymbol{Y}}(M, N, \lambda_0) - \boldsymbol{Y} \right), \tag{21}$$

where the mean value of the difference between the time series of the estimated output and the measured output is obtained with a division by the number of data samples m. The resulting MSE is a square matrix of the size $n_y \times n_y$ with n_y being the number of output channels. Without loss of generality, λ_0 is initially set to 0 in the following, as it its optimal value is unknown at first. Based on the MSE, the log-likelihood function can be expressed as [54]

$$\ln(\hat{L}(M, N)) = -\frac{m}{2} \left(\ln(\det(\text{MSE}(M, N))) + 1 + n_y \ln(2\pi) \right). \tag{22}$$

Using the log-likelihood function, the quality of the estimation is assessed by employing the Akaike information criterion (AIC)

$$\text{AIC} = -2 \ln(\hat{L}) + 2(M + N) n_x n_y \tag{23}$$

where $(M + N)n_x n_y$ denotes the number of model parameters. The term $n_x n_y$ expresses the number of distinct finite impulse response filters as the product of input channels n_x multiplied by the number of output channels n_y. Since interpolated FIR filters are employed, it is not entirely clear which value to use for the model order of the individual filters. We propose utilising the sum $M + N$ that relates to the dense filter order and the number of sparse filter taps as stated in Equation 23. Since $M \gg N$, the addition of N can be interpreted as a penalty applied to models with excessively large numbers of filter taps.

It should be noted at this point that, similar to the AIC, other filter order selection or information criteria can be employed [55]. Nevertheless, we propose the using the AIC, as, in the presented applications, it led to the most reasonable models. To obtain values for the parameters M and N, a sweep through the parameter space is conducted by application of a grid sampling. At every sampling point, the identification method is applied and subsequently the AIC is evaluated. The resulting AIC values yield a two-dimensional convex surface as a function of M and N. The global

16

minimum of this surface then yields the parameters with the minimum associated information loss and thus the optimal model.

In a second step, the last free identification parameter λ_0 is determined based on the previously determined values of M and N. To this end, the generalised cross-validation (GCV) [56]

$$\text{GCV}(\lambda) = \frac{\left\| \hat{\boldsymbol{Y}}(\lambda_0) - \boldsymbol{Y} \right\|^2}{\left| \text{tr} \left(\boldsymbol{I} - \tilde{\boldsymbol{T}} \left(\tilde{\boldsymbol{T}}^\mathsf{T} \tilde{\boldsymbol{T}} + \lambda \boldsymbol{I} \right)^{-1} \tilde{\boldsymbol{T}}^\mathsf{T} \right) \right|^2} \tag{24}$$

is employed. The GCV function has a global minimum at the value for λ_0 which is the best compromise between accuracy and avoidance of overfitting. To obtain this minimum, a sweep over the parameter λ_0 is conducted and the setting associated with the minimal GCV is selected.

2.5. Computational performance

The evaluation of Equation 19 is computationally intensive, due to the matrix multiplication $\tilde{\boldsymbol{T}}^\mathsf{T} \tilde{\boldsymbol{T}}$. The computational complexity is of the order $\mathcal{O}(mN^2)$, where m is the number of measurement data samples and N is the number of filter taps. Due to the quadratic influence N, the number of filter taps should be as low as possible to minimise computing times. This is valid under the assumption that the number of measurement data samples is much greater than the filter order, i.e. $m \gg M$.

Further, the shift matrix $\tilde{\boldsymbol{T}}$ takes up more memory than typically available on a desktop computer, even for small numbers of measurement samples. This slows down the computation of $\tilde{\boldsymbol{T}}^\mathsf{T} \tilde{\boldsymbol{T}}$, because the speed of this matrix multiplication is limited by the memory bandwidth. To reduce the size of the shift matrix $\tilde{\boldsymbol{T}}$, Equation 18 is computed in a batch operation for small chunks of measurement data. The terms $\tilde{\boldsymbol{T}}^\mathsf{T} \tilde{\boldsymbol{T}}$ as well as $\tilde{\boldsymbol{T}}^\mathsf{T} \boldsymbol{y}$ can thus be summed up iteratively to minimise the computing time. Hence, the batches can be processed independently, which enables parallel computation and thus increases the efficiency on many-core computers.

Due to the relatively low dimension of $\tilde{\boldsymbol{T}}^\mathsf{T} \tilde{\boldsymbol{T}}$, the matrix inversion in Equation 19 has an insignificant impact on the computing time when long measurement data time series are employed. Hence, no special consideration of performance aspects is required for the matrix inversion.

2.6. System theoretical considerations

The system properties stability, controllability, observability and invertability are important for the practical usefulness of the multiple-input/multiple-output IFIR filter topology. Since the filter

17

structure utilised in the identification process is based on FIR filters, most of its properties are identical to FIR filters. In terms of the z-transformation, the structure of a single-input/single-output FIR filter can be expressed as

$$G(z) = \frac{b[0] + b[1]z^{-1} + b[2]z^{-2} + \ldots + b[M]z^{-M}}{1}, \tag{25}$$

where $G(z)$ is the transfer function and $b[0...M]$ are the coefficients of the FIR filter. The denominator of the transfer function is unity, which indicates that the filter has no poles and is thus unconditionally stable. To examine the controllability and observability, the state-space model of a single-input/single-output system is formulated

$$\boldsymbol{x}_{\mathrm{ss}}[i+1] = \boldsymbol{A}_{\mathrm{ss}}\boldsymbol{x}_{\mathrm{ss}}[i] + \boldsymbol{b}_{\mathrm{ss}}x[i]$$
$$y[i] = \boldsymbol{c}_{\mathrm{ss}}^{\mathsf{T}}\boldsymbol{x}_{\mathrm{ss}}[i] + d_{\mathrm{ss}}x[i], \tag{26}$$

where $\boldsymbol{A}_{\mathrm{ss}}$ is the $(M \times M)$-dimensional state matrix, $\boldsymbol{b}_{\mathrm{ss}}$ is the input vector, $\boldsymbol{c}_{\mathrm{ss}}^{\mathsf{T}}$ is the output vector and d_{ss} is the feedthrough factor. The input time series x and the output time series y are incorporated into the system using the time step i. In order to represent a FIR filter, the parameters are set to

$$A_{\mathrm{ss},kl} = \delta_{k-1,l} \qquad b_{\mathrm{ss},k} = \delta_{k,1}$$
$$c_{\mathrm{ss},l}^{\mathsf{T}} = b[l+1] \qquad d_{\mathrm{ss}} = b[0], \tag{27}$$

where the Kronecker delta function δ is used to describe the contents of $\boldsymbol{A}_{\mathrm{ss}}$ and $\boldsymbol{b}_{\mathrm{ss}}$. In this formulation, the state space matrix $\boldsymbol{A}_{\mathrm{ss}}$ has ones on the lower secondary diagonal and is zero otherwise. This means that the entire internal state is shifted in each time step. The input vector $\boldsymbol{b}_{\mathrm{ss}}$ feeds the most recent input $x[i]$ to the beginning of this delay line. The output vector $\boldsymbol{c}_{\mathrm{ss}}^{\mathsf{T}}$ contains the coefficients $b[j]$ of the FIR filter, starting from the second coefficient. Since the first coefficient $b[0]$ of the filter needs to be applied without any delay, it is contained in the feedthrough factor d_{ss}. The controllability matrix following from this state space representation is $\boldsymbol{\mathcal{C}} = [\boldsymbol{b}_{\mathrm{ss}} \quad \boldsymbol{A}_{\mathrm{ss}}\boldsymbol{b}_{\mathrm{ss}} \quad \cdots \quad \boldsymbol{A}_{\mathrm{ss}}^{M}\boldsymbol{b}_{\mathrm{ss}}] = \boldsymbol{I}$, meaning that the output is unconditionally controllable. The observability matrix $\boldsymbol{\mathcal{O}} = [\boldsymbol{c}_{\mathrm{ss}} \quad \boldsymbol{A}_{\mathrm{ss}}^{\mathsf{T}}\boldsymbol{c}_{\mathrm{ss}} \quad \cdots \quad (\boldsymbol{A}_{\mathrm{ss}}^{M})^{\mathsf{T}}\boldsymbol{c}_{\mathrm{ss}}]^{\mathsf{T}}$ only has full rank if all filter coefficients are non-zero, in which case the system is observable as well.

Since there are no restrictions imposed on the filter coefficients contained in $\boldsymbol{c}_{\mathrm{ss}}$, the zeros of Equation 25 are usually not bounded to the unit circle. This means that an inverse filter obtained by flipping the numerator and denominator of the transfer function is generally unstable. However,

18

it is possible to obtain a stable least-squares optimal inverse finite impulse filter using Equation 8 [35].

3. Structural measurements of a timber building

To validate the identification scheme outlined in the previous sections, measurement data was obtained from a timber building under construction. The building shown in Figure 6 has six floors, of which the first floor slab is built from concrete and the upper floor slabs are made from cross-laminated timber. The walls of the upper floors are carried out using a timber frame construction. The ceiling height is 2.7 m and the total height of the building is 23 m. As illustrated in Figure 7, the building is situated close to several railway tracks, with traffic from commuter and long-distance trains. Figure 7 contains the site plan including some dimensions for reference.

Figure 6: Photograph of the timber building and the railway embankment in Berlin, Germany.
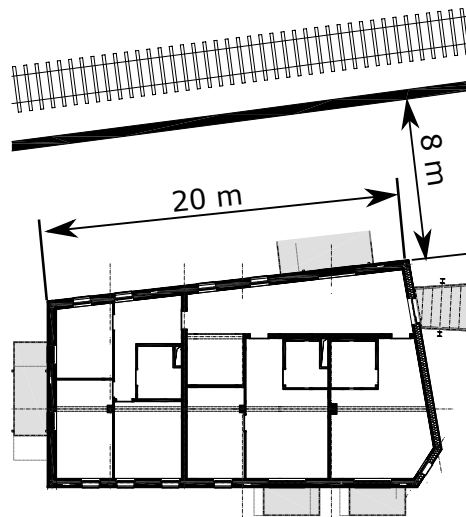
Figure 7: Site overview with railway tracks and floor plan of the building.

In Section 3.1 we introduce the sensor positions and the data acquisition setup which was used for the in-situ measurement. Further, in Section 3.2 we characterise the structural dynamics by examining the structural eigenmodes of individuals floors and of the building as a whole. The data sets captured using the measurement setup as well as the train types are discussed in Section 3.3.

19

3.1. Measurement setup

During the measurement campaign, the building was equipped with a measurement setup consisting of multiple triaxial as well as uniaxial geophone sensors. The sensor distribution inside the building is similar to those presented in previous studies, such as Sanayei et al. [23] or Mugabo et al. [9]. Triaxial geophones were placed in the soil, on the ground level and on several floors. The structure was additionally equipped with uniaxial sensors which measure vibrations in the vertical direction.

The sensors are aligned according to a global coordinate system depicted in Figure 8. The measurement directions $\boldsymbol{d}_1$ and $\boldsymbol{d}_2$ cover vibrations in the horizontal plane, while $\boldsymbol{d}_3$ points in the vertical direction. Figure 8 also shows the placement of the sensors on the ground level and on the fourth and fifth floor. For the measurement of soil vibrations, one triaxial geophone is positioned in the soil at position G near the east corner of the building. The building has no basement, so the foundations coincide with the ground level floor, which is a reinforced concrete slab. A triaxial geophone is thus placed at location E on the ground floor close to the soil geophone to capture the difference between soil and foundation vibrations. Two additional uniaxial geophones are placed on the ground level near load-bearing walls at locations S and N. The floors four and five are each equipped with two triaxial geophones at the location S and W on the two main ceiling panels of the building, as marked in Figure 8. On the second floor, one triaxial geophone was located at location W and additionally three uniaxial sensors were installed. The first floor is constructed using reinforced concrete, so it is of minor interest to the topic at hand. Hence, only two vertical measurement channels are present at the N and S positions on the first floor. The 32 measurement channels, the sensor configuration and their distribution are summarised in Table 1.

The geophone sensors are of type SM-6 and have a sensitivity of $27\,\mathrm{Vs/m}$. Due to the physical measurement principle, different versions are required for the horizontal and vertical measurement directions. The sensors have a cut-off frequency of $4.5\,\mathrm{Hz}$ and are connected to equalising pre-amplifiers to achieve a linear frequency response down to $1.0\,\mathrm{Hz}$. The pre-amplifiers are connected to a central data acquisition system, which synchronously records all 32 channels at a sampling frequency of $1000\,\mathrm{Hz}$. Calibration of individual sensors is achieved using adjustable gain and frequency response settings of the pre-amplifiers.

Photographs of triaxial soil and floor sensor measurement setups are displayed in Figure 9. The three spacial directions are measured separately using individual sensors, which are manually
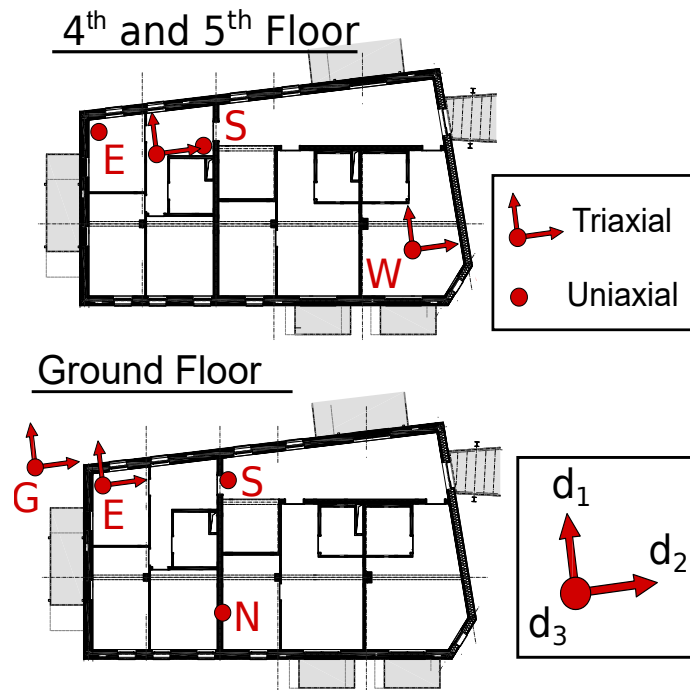
20

Figure 8: Measurement positions in the soil, on the ground floor, the fourth and the fifth floor of the building. The locations are marked for soil (G), west (W), east (E), north (N) and south (S). The global coordinate system is indicated by a triad.

aligned according to the global coordinate system. The soil sensors are anchored using a 50 cm long pole driven into the ground. The individual geophone sensors are equipped with mounting plates featuring three spikes to establish a firm connection with the floor slabs.

Table 1: Sensor setup for soil and individual building floors, sensor placement indicated using capital letters.

Level	Uniaxial Vertical	Triaxial	Number of Channels
Soil	-	1×3 (G)	3
Ground Floor	2 (S,N)	1×3 (E)	5
1st Floor	2 (S,W)	-	2
2nd Floor	3 (S,E,E)	1×3 (W)	6
4th Floor	2 (S,E)	2×3 (E,W)	8
5th Floor	2 (S,E)	2×3 (E,W)	8
Total	11	7×3	32
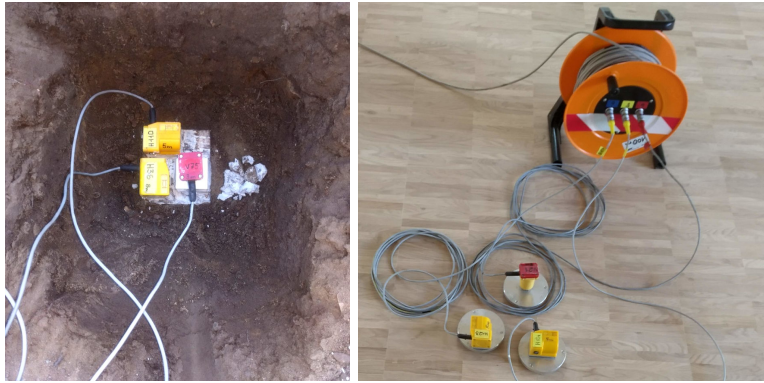
Figure 9: Photographs of triaxial measurement positions. Left image shows setup placed on a pole at location G. Right image shows setup on the floors.

3.2. Structural dynamics

The building exhibits two families of vibration modes as illustrated in Figure 10. One family of modes is linked to the vertical vibration of the floor slabs. In these modes, the floor panels vibrate vertically on each floor of the building, causing almost no movement of the walls. The second family of modes includes the shear modes of the building, in which the building floor slabs move in the horizontal plane as rigid bodies, causing the walls to bend. This assertion stems mainly from the observations made using the filters identification discussed in the proceeding chapters. However, in preliminary studies not included in this paper, the modal behaviour of the structure was also validated using operational modal analysis.
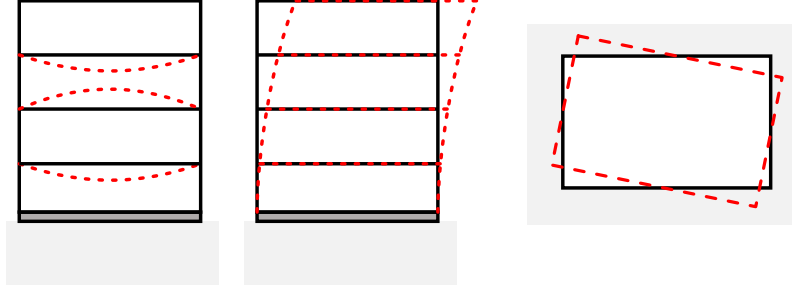
Figure 10: Sketch of the main mode shapes of a building. Structure at rest shown in black, deformed structure shown in red. Left panel: vertical floor slab mode sectional view. Centre panel: horizontal shear mode sectional view. Right panel: torsional mode top view.

Due to the placement of load-bearing walls and beams, the floor slabs have a complex frequency response. Some modes are localised to individual panels, other modes correspond to movements across the whole floor slab. This means that no single mode can be identified as the main mode of vibration in the vertical direction.

The horizontal behaviour of the structure is dominated by two pronounced modes at about 2 Hz and 6 Hz. The corresponding modeshapes resemble bending modes of a cantilever beam as shown in the centre panel of Figure 10. However, these horizontal modes also exhibit rotational movement of the floor slabs which leads to additional torsional and shear deformations. Similar results were obtained by Mugabo et al. [9] when studying the eigenfrequencies of a cross-laminated timber structure.

3.3. Measurement data sets

Several measurement time series of varying length were obtained, each containing data from one or more passing trains. The measurement was carried out during ongoing interior fitting construction work, so the data also contains vibrations originating from construction machinery as well as floor slab vibrations induced by personnel working at the site. Such a signal contamination is typical for dynamic measurements in buildings, where vibration sources are not as controllable as in laboratory setups.

There are two train types present in the data, which were recorded with a high quality: long-distance trains and commuter trains. The data sets captured during the measurement campaign are summarised in Table 2. Some regional trains also passed by during the measurement campaign,

23

Table 2: Data sets recorded during measurement campaign.

Train type	Number of trains	Accumulated measurement time in s
Long-distance	5	360
Commuter	14	993
Total	19	2170

however, due to a high variability in the configuration of the trains and poor data quality due to several trains passing at the same time, these are left out of the analysis. The train tracks were observed visually from the construction site, however no accurate information about the configuration of the trains, or the properties of the tracks was available for this study.

4. Filter identification

The measurement data is used to obtain multiple-input/multiple-output FIR filters considering the selected train types as vibration sources. Using the method presented in Section 2, we identify filter coefficients which model the transmission from the soil to individual building floor slabs, as well as the transmission from the foundation to the building floor slabs. Since the multiple-input/multiple-output identification generates an immense number of individual FIR filters, in the following sections, the properties of the identification method are presented using exemplary measurement channels only. Nonetheless, we verified our conclusions by analysing the results for the full set of channels and filters.

To discuss the filter identification, we limit ourselves to a setup with a triaxial input and a triaxial output. The triaxial soil geophone is therefore chosen as the input of the filter model the triaxial geophone on the west side of the fifth floor is chosen as the output, which are marked as G and W in Figure 8. This sensor combination represents the longest path of transmission through the building and thus exhibits a complex transfer behaviour. The identification is carried out using a concatenation of the time-domain measurement data sets for long-distance trains.

To obtain frequency-domain data, Welch's power spectral density estimation [43] is used for time series data as well as for filter coefficients. We consistently apply a window size of 2048 samples and an overlap of 1024 samples to obtain high-resolution spectra with sufficient smoothing.

In this section, measured sensor signals as well as identified impulse response filters are discussed

24

in detail. We analyse the results both in the time domain and in the frequency domain. The filter order selection is detailed in Section 4.1 and the numerical performance is discussed in Section 4.4. Section 4.3 discusses the stability of the identification with respect to the parameters M, N and λ_0. Finally, Section 4.2 is about the identification of filter coefficients and the structural dynamic interpretation.

4.1. Filter order selection

In this section, we analyse how the identification parameters M, N and λ_0 influence the resulting finite impulse responses using measurement data obtained for long-distance trains. The parameters M and N are determined by searching for a minimum of the AIC. As illustrated in Figure 11, the location of the minimum AIC value is located at $M = 6500$ and $N = 550$. To determine the normalised regularisation parameter λ_0, the GCV approach is used. The GCV function displayed in Figure 12 shows that the minimum is close to $\lambda_0 = 1.0$. The AIC and GCV functions were sampled using a uniform grid, as displayed in Figures 11 and 12. The minima were then determined by searching for the minimum value among the sampled points.
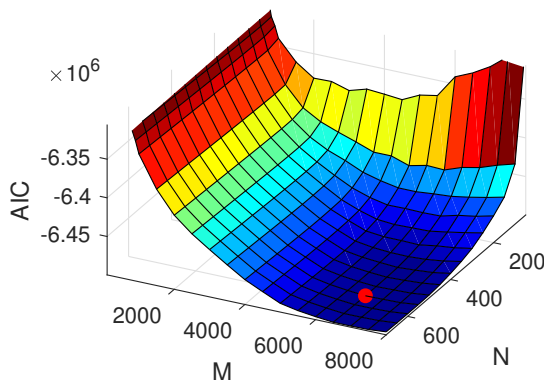
Figure 11: Plot of the AIC over the identification parameters M and N. The minimum is highlighted by a red dot.
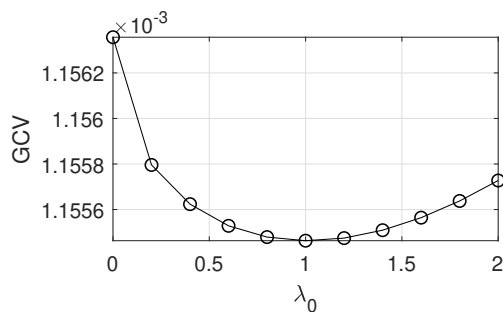
Figure 12: Plot of the generalised cross validation over the regularisation parameter λ_0.

The coefficients of an exemplary identified FIR filter for the transmission from the soil $\boldsymbol{d}_2$-direction to the fifth floor $\boldsymbol{d}_1$-direction are shown in Figure 13. As the impulse response has decayed significantly up to coefficient 6000, the automatically determined parameter $M = 6500$ seems to be a reasonable choice.
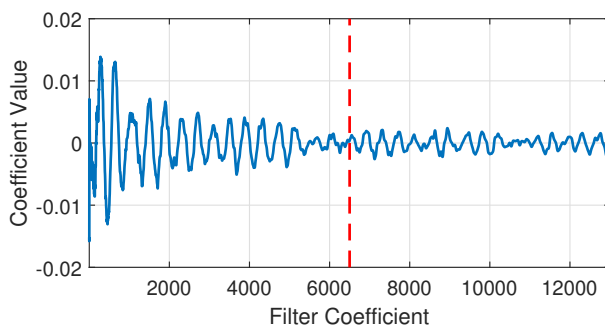
25

Figure 13: Effect of filter order $M + 1$ on the impulse response and filter order determined using AIC ($M = 6500$).

Spectra for several settings of the parameter N are shown in Figure 14 to illustrate its influence on the high frequency response. The number of filter taps $N + 1$ should be chosen as low as possible because of its high impact on the computational performance. However, when the density of filter taps is too low, the high-frequency response drops off significantly. Hence, the filter model will underpredict the actual vibration amplitude, as evident in the graph shown for $N = 275$ in Figure 14.
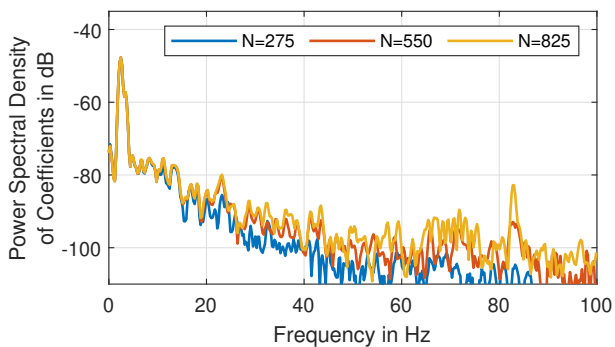
Figure 14: Effect of the number of filter taps $N + 1$ on the frequency response of the identified filters.

The normalised regularisation parameter λ_0 has to be selected such that high-frequency artefacts are suppressed without significantly reducing the amplitude of the prognosis time series. This is illustrated in Figure 15, where both the impulse response time series as well as the power spectral density of different settings are compared. The application of smoothing leads to a decrease in high-frequency response, which is desired to remove overfitting, as shown for the $\lambda_0 = 1.0$ case in Figure 15. However, if too much smoothing is applied, the low-frequency response diminishes

26

as well, which leads to an underprediction of the vibration level by the identified filters. This is illustrated by the $\lambda_0 = 10$ graphs in Figure 15, where significant power is missing above 20 Hz.
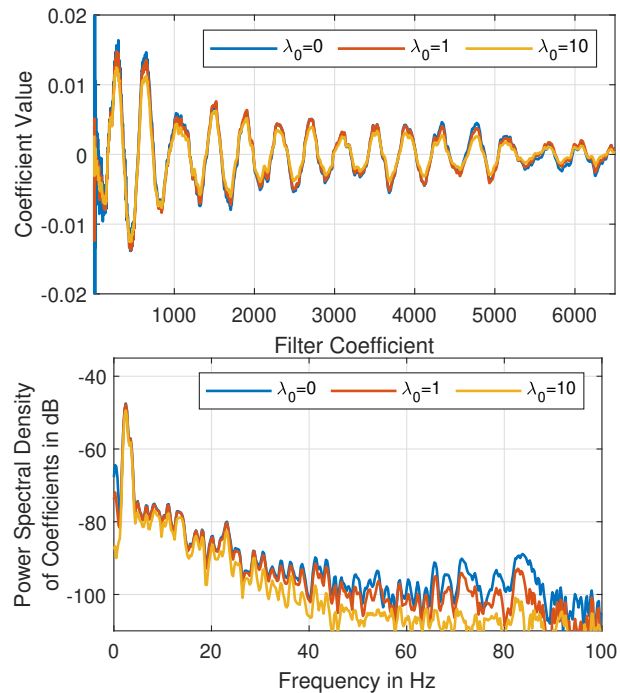

Figure 15: Influence of the normalised regularisation parameter λ_0 on the identified filters, in terms of time-domain as well as frequency-domain response.

In conclusion, the choice of parameters is of major importance for obtaining good identification results. A reasonable set of parameters can be provided automatically by the procedure outlined in Section 2.4.

4.2. Identification of multiple-input/multiple-output filters

The 3×3 array of impulse responses identified between the two triaxial sensor positions is shown in Figure 16. Each row in this plot belongs to one measurement direction of the soil geophone. The columns belong to the directions of the fifth-floor geophone marked with a W in Figure 9. In all of the impulse responses, the signal amplitude decays over time, as is expected for a damped mechanical system. Each of the fifth-floor measurement directions has a different dominant resonance frequency. These resonance frequencies correspond to the eigenmodes of the floors and the shear modes of the building, as discussed in Section 3.2. The cycle duration of the vertical d_3-direction is much shorter,

27

when compared to the horizontal directions. The reason for this difference is that it belongs to a floor slab resonance frequency, which is considerably higher than the frequencies of the horizontal
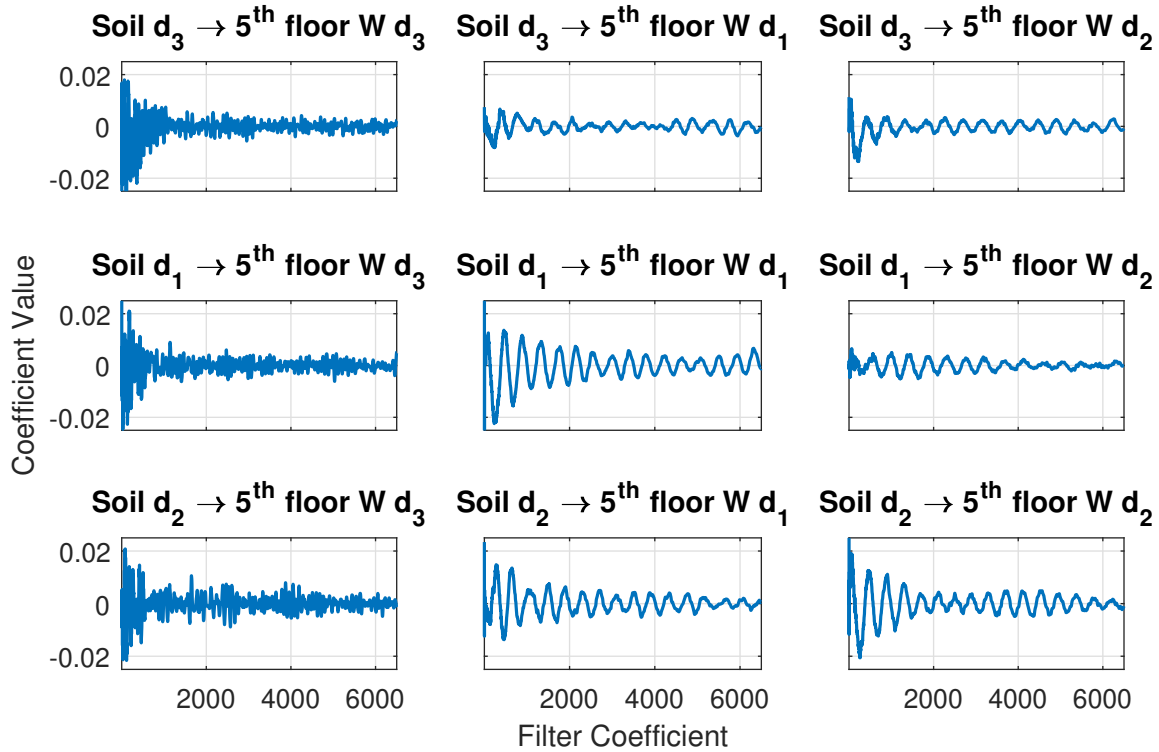
545 shear modes.

Figure 16: Coefficients of the impulse response filters contributing to the prognosis of a fifth-floor triaxial sensor. The input signal is taken from the triaxial soil geophone.

The frequency-domain response of the filters is depicted in Figure 17. For the horizontal d_1 and d_2-directions on the fifth floor, a sharp peak can be observed near $3\,\mathrm{Hz}$, which belongs to the building's shear modes. The spectra for the d_3-direction indicate several resonance peaks in the range between $10\,\mathrm{Hz}$ and $20\,\mathrm{Hz}$, which belong to individual floor vibration modes.

28
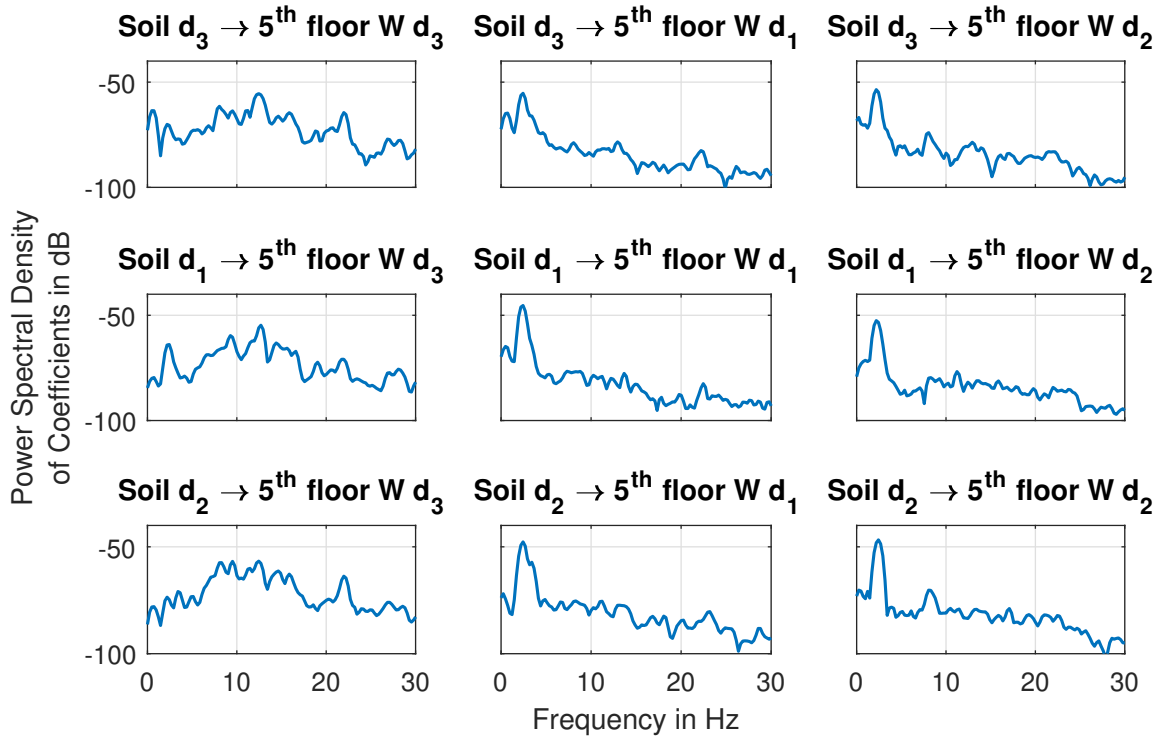
Figure 17: Spectra corresponding to the impulse response filters shown in Figure 16.

4.3. Robustness of IFIR coefficient identification

The robustness of the proposed identification method is assessed by conducting a Monte Carlo variation of the identification parameters. Therefore, each of the parameters M, N and λ_0 is randomised using a uniform distribution of $\pm 10\%$ of the original values. The filter coefficients are identified for the resulting multi-variate parameter distribution using 20 realisations. Figure 18 illustrates the distribution of the impulse responses, highlighting the stability of the identification method.

The detail view in Figure 18 shows that an appreciable amount of statistical scatter is introduced. However, considering the FIR filter as a whole, the sensitivity with respect to the variation of the identification parameters is quite low. In case of transient impulses at the inputs, the peak output amplitude of the identified filters varies by about $\pm 5\%$. For the practical applicability of the method, we deduce that it is adequately stable, meaning that it is not necessary to put too much time and effort into determining the numerical values of the identification parameters.
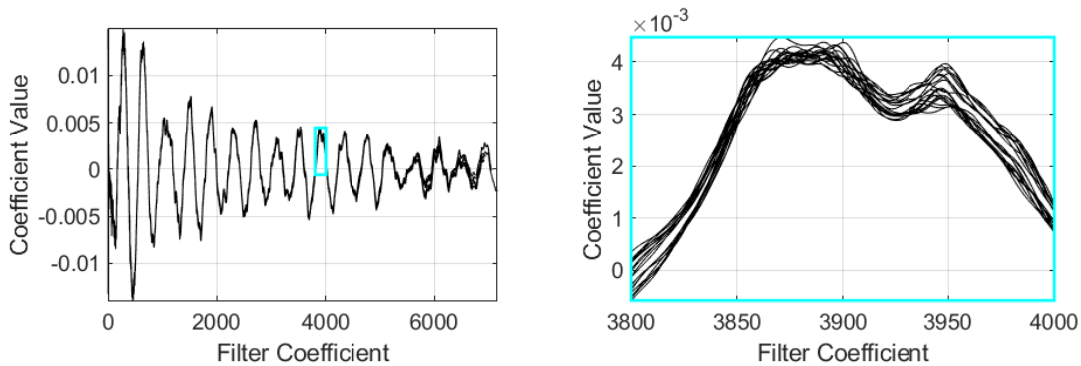
29

Figure 18: Identified filter coefficients (left) and detail view (right) considering Monte Carlo variation of the identification parameters.

4.4. Numerical performance

The numerical performance of the presented identification approach for dense and interpolated FIR filters is compared to the `impulseest` function from the MATLAB System Identification toolbox [37], which implements the identification algorithm described by Chen et al. [36]. The same data as used in Section 4.1 is employed for this purpose. As the numerical complexity of the identification procedure is mainly dependent on the number of FIR filter coefficients $M+1$, this parameter is used as the baseline for the comparison. The runtime of the `impulseest` function, a dense FIR estimation and the interpolated FIR estimation with $N = 0.1M$ is shown in Figure 19.
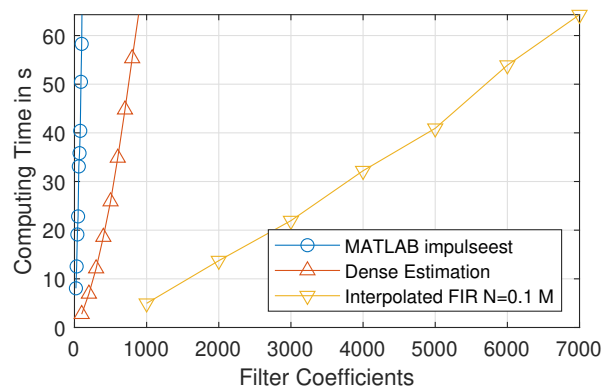

Figure 19: Comparison of numerical performance of MATLAB's `impulseest` function with the presented methods.

The comparison was carried out using a quad-core processor running at $3.3\,\mathrm{GHz}$. The results show that the interpolated FIR method has to be employed to reach the optimal filter order $M =$

30

6500 with manageable computing times. Both the dense estimation as well as the MATLAB function `impulseest` exhibit an insufficient numerical performance for such high numbers of filter coefficients. As demonstrated in Figure 20, the estimation quality is mainly dependent on the number of filter coefficients employed. Hence, the high numerical performance of the IFIR method yields the lowest estimation errors.
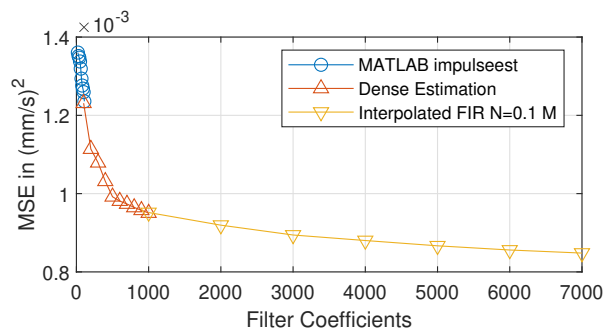

Figure 20: Mean squared error comparison of MATLAB's `impulseest` function with the presented methods.

5. Vibration prognosis

In this section, the multiple-input/multiple-output identification method is used to perform vibration prognosis based on the measurement data sets. In Section 5.1, we examine how accurate the prognosis can potentially become in case of high numbers of input channels. A discussion on the difference in the prognosis accuracy, which is achieved when using soil or ground floor vibrations as an input, can be found in Sections 5.2 and 5.3. Further, we investigate whether vibration transfer models derived for a specific type of train are transferable to another train type in Section 5.4. Finally, in Section 5.5, we introduce a virtual sensing concept using the vibration prognosis method.

5.1. Prognosis using high numbers of input channels

To assess the potential accuracy of a prognosis based on multiple-input FIR filters, we employ a very high number of input channels. The filter models are derived using all data sets that were obtained for passing commuter trains since most data sets are available for this train type. Every sensor installed below the fifth floor is used as an input channel in order to obtain a prognosis for the fifth-floor triaxial sensor located at the west side of the building. This way, impulse responses

31

for 24 input channels and three output channels are derived, leading to a filter model consisting of 72 individual FIR filters.

595   We use data from a different train type for verification of the prognosis and for the identification. This way, we make sure that potential overfitting issues are easily discovered. Since the filter model is identified using commuter train data, an excerpt of the time series measured for long-distance trains is used to demonstrate the numerical results. Figure 21 shows a comparison of the prognosis and the triaxial measurement data corresponding to the maximum amplitudes recorded from a

600 passing long-distance train. As can be expected from the spectra shown in Figure 17, the vertical d_3-direction exhibits a much higher fundamental vibration frequency than the horizontal directions. The prognosis time series matches almost perfectly to the measurement in all channels, suggesting a very high prognosis accuracy.
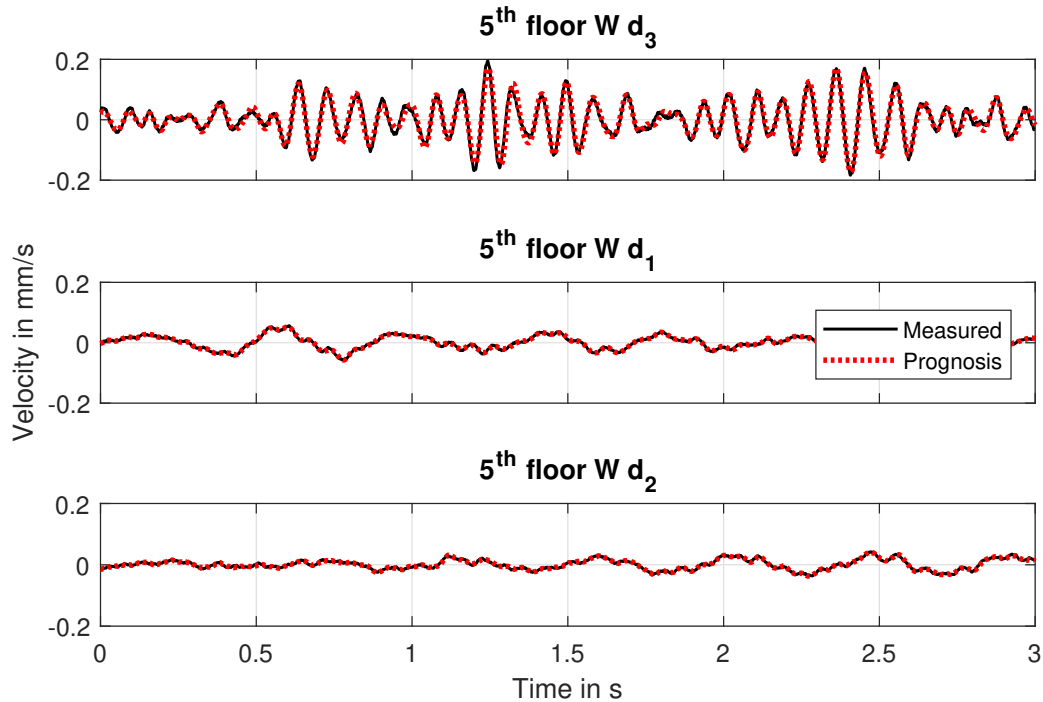

Figure 21: Measured data and prognosis for the fifth floor, considering 24 input channels and excitation by a long-distance train. The filter model used for the prognosis is identified using commuter train data.

    Of course, this numerical example is rather academic, since such a vast array of sensors would

605 hardly be implemented in practice. However, it demonstrates that the prognosis based on IFIR

32

filters indeed can become very accurate, when enough information about the vibration state of the structure is available. The accuracy of the prognosis is also reflected in the frequency domain, as shown in Figure 22. Especially in the frequency range below 20 Hz, where the power spectral density is the highest, the prognosis is in very good agreement with the measurement.
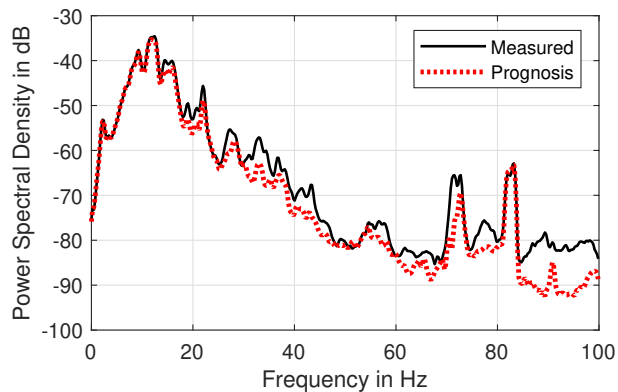

Figure 22: Spectra for measured and prognosis data of the vertical d_3-direction of the fifth floor triaxial sensor located at the west side of the building considering 24 input channels.

In Figure 23, the influence of the number of input channels is examined using the mean squared estimation error. The estimation error drops and converges towards higher numbers of input channels. Above approximately 15 input channels, no significant improvement is achieved. Figure 23 also shows that the estimation error of a single-input prognosis is about six times higher compared to the 15 sensor case, which demonstrates the advantage of the multiple-input topology.
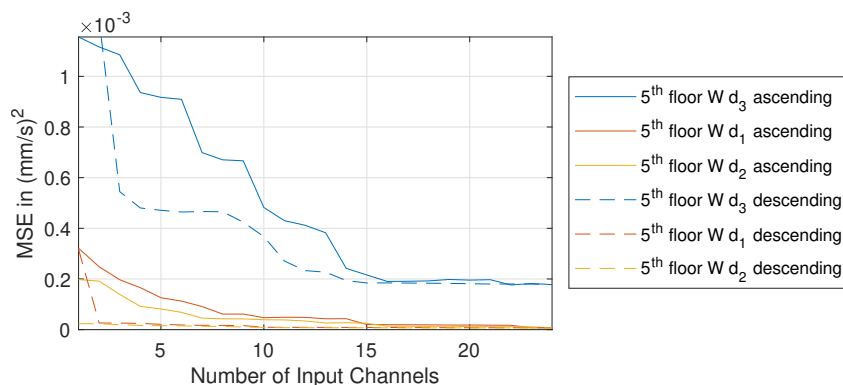
33

Figure 23: Mean squared error (MSE) metric of the fifth floor triaxial sensor channels on the west side with respect to the number of input channels used for the identification. Channels are sorted based on the floor number, starting at the soil/ground level. MSE is reported for both ascending and descending order.

5.2. Prognosis based on soil vibration data versus ground floor vibration data

In this section, a more practical case is regarded, where we use soil and ground floor vibration data as an input for the prognosis of the second floor time series. Therefore, we investigate the influence of the position of input measurement sensors on the accuracy of the resulting prognosis. To eliminate any influence of the train types, the prognosis is carried out using the same commuter train data as for the identification. The second floor sensor is chosen as the output to exemplify the horizontal shear modes of the building.

The comparison is carried out using input data from the soil and ground floor triaxial sensors, indicated as G and E in Figure 9. The sensors are located only a few metres apart, however the ground floor sensor is directly coupled to the structure and thus able to capture more information about the vibrational state of the building. We illustrate this assertion in Figure 24 using the measured and predicted power spectral density spectrum of the second floor in the horizontal d_2-direction. The left panel of the figure shows a detailed view of the range from $0\,\mathrm{Hz}$ to $20\,\mathrm{Hz}$, which is most relevant for vibration assessment, as is contains the peaks belonging to the two dominating shear modes. These peaks are very pronounced since the low-frequency horizontal modes exhibit significantly less damping than the vertical floor slab modes. The right panel shows the spectrum up to $100\,\mathrm{Hz}$, where much of the vibration signal is caused by construction machinery present at the site. While both prognoses systematically underpredict the measured spectrum, the prognosis based on the ground floor sensor matches the measured signal better than the prognosis using the

34

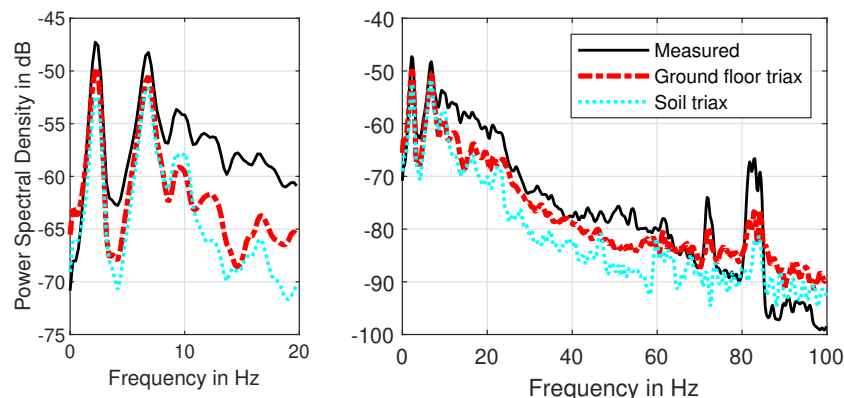soil sensor. The difference is small up to 10 Hz and increases with higher frequencies.

Figure 24: Comparison of second-floor horizontal measured spectra with those obtained from prognosis using a triaxial soil sensor and triaxial ground floor sensor, respectively. The filter model is identified using and applied to commuter train data.

5.3. Time-domain analysis for different input sensor locations

In this section, the estimation performance is assessed in the time domain according to the vibration assessment criterion defined by the German standard DIN 4150-2 [2]. In this standard, the weighted vibration signal $\mathrm{KB_F}$ is used to classify the comfort level based on a measured vibration time series. It is calculated by initially applying a frequency weighting to the vibration velocity, which models human perception of the disturbance caused by the vibration. In the discrete-time z-transform representation, the velocity time series $y(z)$ is weighted using a first-order high-pass filter with a cutoff frequency of 5.6 Hz

$$\alpha_{\mathrm{HP}} = e^{-2\pi \cdot 5.6\,\mathrm{Hz}/f_S} \tag{28}$$

$$\mathrm{KB}(z) = \frac{\alpha_{\mathrm{HP}} - \alpha_{\mathrm{HP}} z^{-1}}{1 - \alpha_{\mathrm{HP}} z^{-1}} y(z), \tag{29}$$

where α_{HP} is the time-discrete filter coefficient, f_S is the sampling frequency and $\mathrm{KB}(z)$ is the weighted signal. The time series KB is used to obtain a first-order low-pass filtered effective amplitude, which results in the $\mathrm{KB_F}$ time series

$$\alpha_{\mathrm{LP}} = e^{-1/(f_S \cdot 0.125\,\mathrm{s})} \tag{30}$$

$$\mathrm{KB_F}^2(z) = \frac{1 - \alpha_{\mathrm{LP}}}{1 - \alpha_{\mathrm{LP}} z^{-1}} \mathrm{KB}^2(z), \tag{31}$$

35

where α_{LP} is the low pass filter coefficient based on a time constant of $0.125\,\mathrm{s}$. The squaring of $\mathrm{KB}(z)$ and $\mathrm{KB_F}(z)$ serve to obtain a moving average of the absolute amplitude instead of the signed amplitude. The $\mathrm{KB_F}$ values are obtained by taking the square root of $\mathrm{KB_F}^2(z)$, resulting in a time series relating to the vibrational energy contained in the signal.

To exemplify the time-domain prognosis, a $\mathrm{KB_F}$ time series is computed for the signal recorded in the vertical $\boldsymbol{d}_3$-direction of the fourth floor triaxial sensor at the east side of the building considering commuter train data. A sensor position in the east corner of the building is chosen as the output in this example because the ground floor sensors are also concentrated in the east corner of the building. Therefore the sensors used as the input channels for the filter model are located close to the load bearing components which transfer vibration energy to the upper floor slabs which enhances the prognosis quality. An excerpt containing the vibration caused by a passing train and the subsequent decay of the signal is depicted in Figure 25.
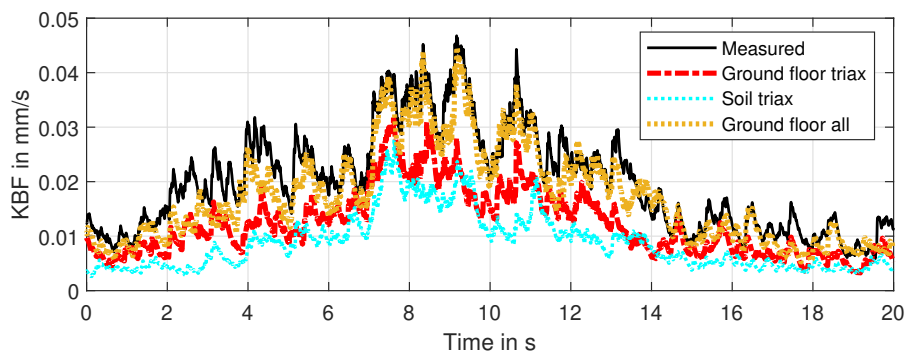

Figure 25: Time series of $\mathrm{KB_F}$ vibration assessment criterion for fourth-floor (E) triaxial sensor vertical $\boldsymbol{d}_3$-direction considering commuter train data. Estimation based on triaxial soil sensor, triaxial ground floor sensor and all five ground floor sensors, respectively.

In addition to the measured signal, the estimation based on the soil triaxial sensor, the ground floor triaxial sensor as well as based on all five ground floor sensors is shown. As discussed in the previous section, the estimation based on the ground floor triaxial sensor fits the measured data better than the estimation based on the soil triaxial sensor. However, both estimations based on the triaxial sensors exhibit an underestimation of the $\mathrm{KB_F}$ amplitude by about a third when compared to the measured data. By taking the two additional vertical sensor positions of the ground floor into account, the estimated time series fits considerably better to the measured data.

36

5.4. Influence of different train types

A question that often arises in the context of vibration prognosis is whether a transfer model derived for one specific excitation source can be utilised when different types of excitation are present. Section 5.1 demonstrates that a highly accurate prognosis can be achieved for long-distance train data when using filters based on commuter train data. However, the number of input channels used in that example is prohibitively high for practical vibration prognosis. In this section, we investigate whether the filter models are transferable using signals recorded for different train types and considering a more practical sensor setup. To characterise the dynamic excitation caused by different train types, we concatenate the time-domain measurement data sets related to long-distance trains and we proceed equally for data associated with commuter trains. Two spectra corresponding to the vertical and a horizontal vibration time series of the ground floor triaxial sensor are shown in Figure 26.
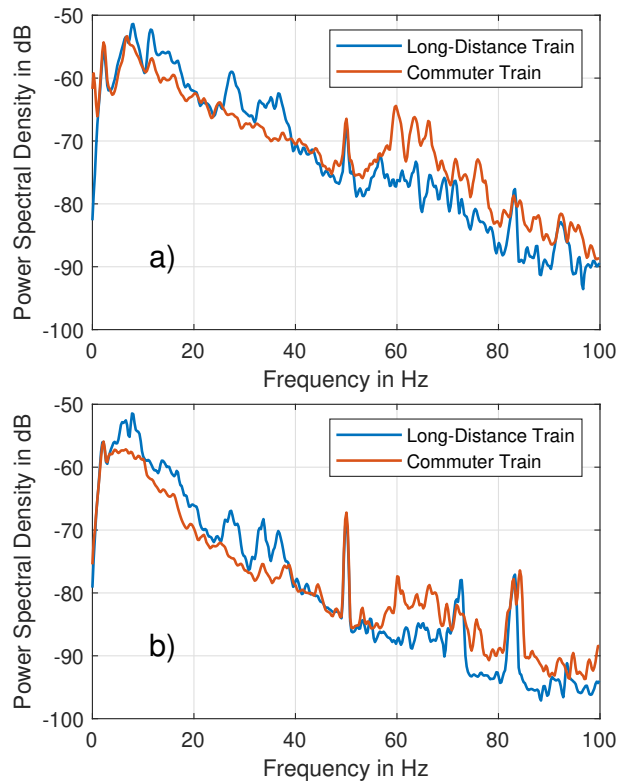

Figure 26: Power spectral density of ground floor triaxial sensor for different train types, a) vertical $\boldsymbol{d}_3$-direction b) horizontal $\boldsymbol{d}_1$-direction

37

The maximum of the signal power is present around 7 Hz for both train types while the power continually drops off towards higher frequencies. The long-distance train spectrum features some peaks below 40 Hz which are not present for the commuter train. In addition to train-induced vibrations, the recorded data contains contamination arising from road traffic vibrations as well as from construction machinery above 60 Hz. Further, a peak at 50 Hz in both data sets indicates cross-talk from power grid wiring, which is most probably caused by poor shielding of the measurement cables.

In the next step, we explore the suitability of filters derived for one train type for the prognosis of a different type of train. For this purpose, we identify FIR filters using long-distance train data and all five ground floor measurement channels as an input. For reference, FIR filters are also identified using the commuter train data. Hence, the commuter train vibration recordings and the long-distance train recordings can be referred to as the training and validation data sets, respectively. In such a setup, it can be expected that the prognosis based on filters derived using commuter train data will be in good agreement with the measurement data. However, the prognosis based on filters derived using long-distance train data will only exhibit correlation with the data if the filter model adequately represents the structural dynamics of the examined timber building. The fourth-floor triaxial sensor located at the east side of the building is used as the data source for the output signals. A comparison of the measured spectra with the prognosis spectra is depicted in Figure 27.

The spectrum for the vertical $\boldsymbol{d}_3$-direction exhibits the maximum amplitude close to 10 Hz, which corresponds to one of the floor eigenfrequencies. In the spectrum for the horizontal $\boldsymbol{d}_1$-direction, the main peak is close to 5 Hz, which corresponds to a building shear mode. Regarding both directions, a good match between measurement and prognosis is achieved up to about 30 Hz. The prognosis based on filters identified using the commuter train data fits better to the measured commuter train spectrum, as can be expected. In the higher frequency range, the vibration levels are much lower and the prognosis accuracy deteriorates.
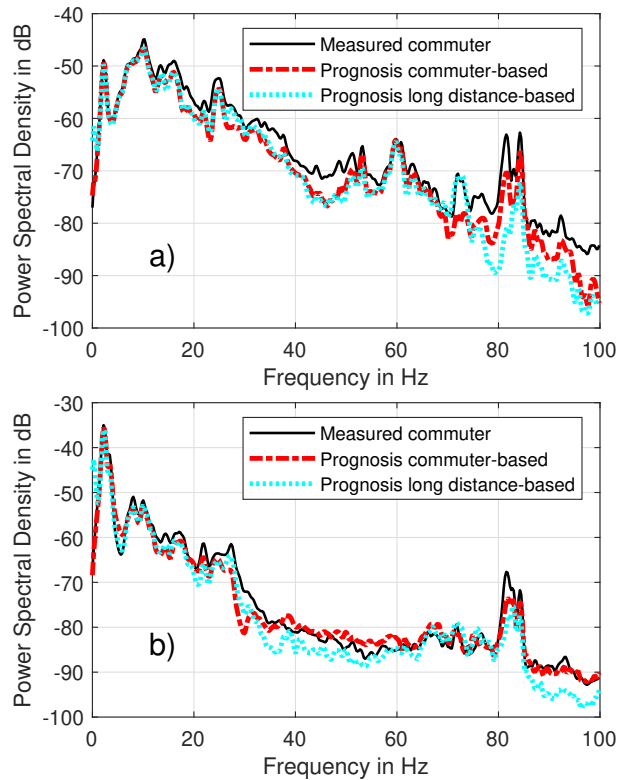
Figure 27: Comparison of measured commuter train spectra with prognosis based on filters identified using commuter (training set) and long-distance train (validation set) data. Filter models identified for transfer from ground floor to fourth floor. Panel a) shows the vertical d_3-measurement direction, panel b) shows the horizontal d_1-direction.

5.5. Virtual sensing and signal contamination

By exploiting the vibration prognosis outlined in the previous chapters, we propose a virtual sensing approach, which can overcome many of the challenges associated with in-situ vibration assessment of buildings. Since the proposed method allows for a high fidelity prognosis considering only the ground floor sensors as an input, it is possible to calculate virtual vibration time series for all other sensor positions. A long-term monitoring campaign can thus be conducted with only the sensors at the ground level being actually equipped and measured. The foundations of buildings are often accessible with minimal intrusion to the apartments, which makes this an acceptable solution for monitoring campaigns which last several days. By monitoring the structure for such extended time periods, the reliability of the vibration assessment can be increased [57], especially when a high variability of excitation is present such as a heavily loaded freight trains passing by night [58].

39

Since the virtual sensors are based on data recorded at the building foundation, signal contamination by the residents of upper floor apartments is avoided. An example for a signal contamination by walking excitation and the prognosis of the corresponding virtual sensor is displayed in Figure 28. The first part of the time series shows that the prognosis and the measured data are largely coincident, as expected for a virtual sensor. A person walks close to the sensor in the highlighted part of the time series, causing a strong vibration event. Figure 28 shows that the ambient vibration has peak amplitudes of about $0.05\,\mathrm{mm/s}$, while the contamination reaches peaks in excess of $0.2\,\mathrm{mm/s}$. Since the vibration signals of the building foundations are not influenced by the person walking on another floor of the building, the virtual sensor is unaffected and thus able to recover the uncontaminated signal.
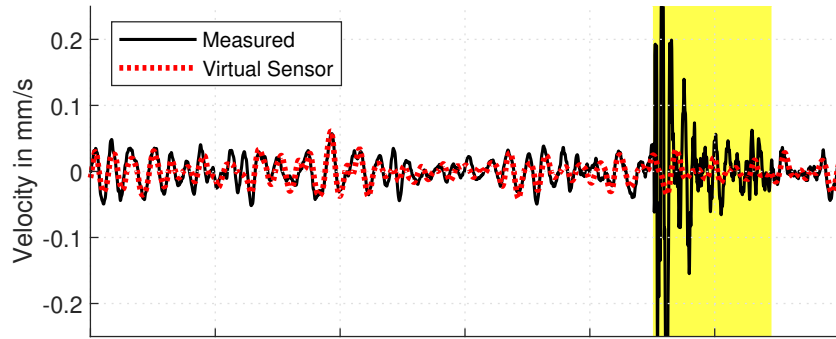

Figure 28: Time series of measured vertical vibration signal of the fifth floor (E) triaxial sensor compared to virtual sensor based on foundation sensor signals. A signal contamination is present in the region highlighted in yellow.

Figure 29 shows the $\mathrm{KB_F}$ time series associated with the signal contamination event shown in Figure 28. This time series was obtained from the velocity measurements using Equation 31. In this example, the $\mathrm{KB_F}$ value of the uncontaminated vibration level stays well below $0.05\,\mathrm{mm/s}$, which is considered to be an excellent comfort level. The measured and the virtual sensor signal align very well in the first part of the time series, indicating that the identified filters accurately capture the vibration response of the building. The contamination in the measured signal leads to a massive increase of the $\mathrm{KB_F}$ value, peaking at $0.13\,\mathrm{mm/s}$, which does not occur in the virtual sensor data.

Such measurement errors are usually identified in a manual process and are subsequently excluded from the vibration assessment. Using the virtual sensing approach, a time series data with less contamination can be obtained which facilitates assessment of long-term monitoring data with
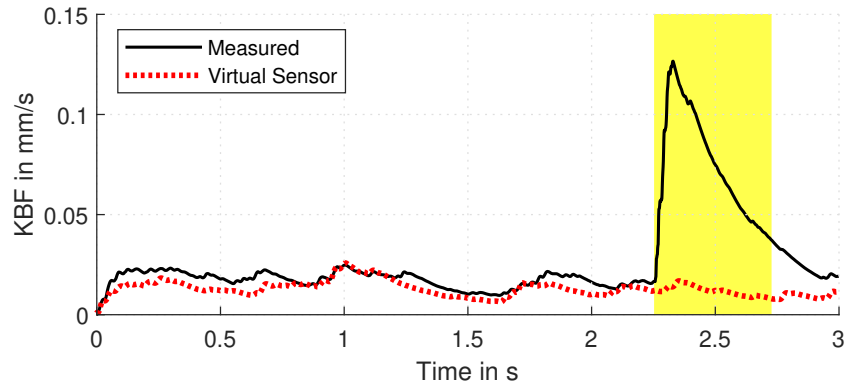
40

Figure 29: Time series of KB_F vibration assessment criterion for signal contaminated by person walking close to sensor.

a high degree of automation. Another possible application of the virtual sensing approach is to provide assistance in the detection of signal contamination. As demonstrated in Figures 28 and 29, the difference between the virtual sensor and the measured signal increases significantly in case of contamination, which can be used as in indication for possible distortion of the recorded data.

6. Benefits and Limitations

The multiple-input/multiple-output filter model adopted for vibration prognosis in this paper is able to generate vibration prognoses, which match measurements much better than prognoses based on a single-input topology, as demonstrated in Section 5.1. However, a drawback of the formulation is the relatively high numerical cost of the filter coefficient identification, especially with large numbers of input channels. The performance was significantly increased by using interpolation functions, as demonstrated in Section 4.4, but improvements may be achieved by further exploiting the mathematical structure of the underlying least squares problem.

The IFIR identification scheme is non-parametric and data-driven, which results in some benefits. For example, a detailed understanding of the structural mechanics, as needed in the methods proposed by Mendes et al. [13] and Sanayei et al. [23], is not required. Further, several previously proposed methods require operational modal analysis [29, 31], which is circumvented by the presented method.

As the presented method is purely data-driven, it can only be used to create vibration prognosis time series for structural designs, which have already been built. This is the case since measurement

41

data of the actual structure is needed to identify the impulse response filters. Thus, in most practical cases, the presented method can not be used to produce a prognosis during the design phase.

Impulse response filters are based on the assumption of linear time-invariant behaviour. In terms of structural dynamics, this mainly means that amplitude-dependent damping effects are not considered [59]. The soil-structure interaction is also greatly simplified by this assumption [60]. Time-invariance can be justified, as ambient excitation exist predominantly, the observation periods are rather short, and within that time, exogenous effects on the dynamics are negligible. This conclusion is substantiated by the excellent accuracy achieved in Section 5.1.

The analysis in Section 5.2 and 5.3 shows that vibration estimation based on ground floor measurement signals leads to significantly increased quality as compared to soil measurement signals. In addition to complex soil-structure interactions which exacerbate accurate prognosis based on soil sensor data, the assumption of time invariance also increases the errors. A passing train changes its location relative to the building while moving on its tracks, so the transmission characteristics change over time. The filter identification method however can only capture the transmission of signals in a time-averaging sense, which inevitably leads to an inaccurate model. This is contrasted by the transmission from the ground floor to the upper levels: Due to the high stiffness of the foundation, its vibrations are much more coherent with the floors of the building than those of the surrounding soil. Hence, the position of the train barely influences the transmission characteristics, so that filters derived on the basis of ground floor vibrations can provide a significantly better prognosis.

When only few sensors are used for the input, the method exhibits a systematic underprediction of the signal amplitude, as evident from the spectra shown in Section 5. This underprediction originates from the least-square identification scheme and is thus inherent to the method. As the number of sensors in a given measurement setup is finite, there is always some contribution of vibration energy which is not captured by any of the sensors. Consequently, the missing energy in the input channels leads to an underprediction of the energy at the output channels. From the standpoint of vibration assessment, this is not ideal, since a conservative method which overestimates the vibration level would be preferable. In practice, this problem can be overcome by estimating the relative prognosis error from a representative measurement data set and by subsequently deriving a safety factor to correct the error.

7. Conclusion and outlook

In this paper, we presented a novel identification method multiple-input/multiple-output IFIR filters. Vibration measurement data was obtained from an existing timber building using sensor positions in the soil, on the ground floor and several upper level floors. The validation of the vibration prognosis using the FIR filters shows that the prognosis method yield adequate accuracy for practical vibration assessments. We were able to identify filter models that can generate reasonable vibration prognosis data for train types, which were not included in the identification data set. The quality of the results shows that the method is reliable even for contaminated data recorded at a construction site. Further, the prognosis method allows the calculation of virtual sensor signals based on real sensors located on the foundations of the building. These virtual sensors enable long-term monitoring campaigns with accurate vibration estimations for all levels of the building.

In future work, the identified FIR filters can be used for the validation of finite element models of timber structures. Such validations can be achieved by directly comparing the impulse response of the simulation model with the FIR filters identified from measurement data. The validated models subsequently enable an improvement of modelling approaches for structural design. Beyond the scope of timber buildings, the identification method is also applicable to other problems involving dynamically loaded engineering structures. For example, the virtual sensor prognosis can be employed for applications such as structural health monitoring and damage localisation [61].

8. Acknowledgments

References

[1] C. Zou, Y. Wang, J. A. Moore, M. Sanayei, Train-induced field vibration measurements of ground and over-track buildings, Science of The Total Environment 575 (2017) 1339–1351. doi:10.1016/j.scitotenv.2016.09.216.

[2] DIN 4150-2, Erschütterungen im Bauwesen; Teil 2: Einwirkung auf Menschen in Gebäuden, Standard, Deutsches Institut für Normung e. V Berlin (1999).

[3] VDI 2038–1, Gebrauchstauglichkeit von Bauwerken bei dynamischen Einwirkungen– Untersuchungsmethoden und Beurteilungsverfahren der Baudynamik, Standard, Verein Deutscher Ingenieure (2012).

[4] R. Brandner, G. Flatscher, A. Ringhofer, G. Schickhofer, A. Thiel, Cross laminated timber (CLT): overview and development, European Journal of Wood and Wood Products 74 (3) (2016) 331–351. `doi:10.1007/s00107-015-0999-5`.

[5] UNECE/FAO, Forest Products Annual Market Review 2018-2019, Forest Products Annual Market Review, UN Geneva Publishing, 2019.

[6] R. Steiger, G. Feltrin, F. Weber, S. Nerbano, M. Motavalli, Experimental modal analysis of a multi-storey light-frame timber building, Bulletin of Earthquake Engineering 15 (8) (2017) 1573–1456. `doi:10.1007/s10518-015-9828-9`.

[7] T. Reynolds, R. Harris, W.-S. Chang, J. Bregulla, J. Bawcombe, Ambient vibration tests of a cross-laminated timber building, Proceedings of the Institution of Civil Engineers - Construction Materials 168 (3) (2015) 121–131. `doi:10.1680/coma.14.00047`.

[8] M. Kawrza, T. Furtmüller, C. Adam, R. Maderebner, Parameter identification for a point-supported cross laminated timber slab based on experimental and numerical modal analysis, European Journal of Wood and Wood Products 79 (2) (2021) 317 – 333. `doi:10.1007/s00107-020-01641-7`.

[9] I. Mugabo, A. R. Barbosa, M. Riggio, J. Batti, Ambient vibration measurement data of a four-story mass timber building, Frontiers in Built Environment 5 (2019). `doi:10.3389/fbuil.2019.00067`.

[10] Z. Tao, Y. Wang, M. Sanayei, J. A. Moore, C. Zou, Experimental study of train-induced vibration in over-track buildings in a metro depot, Engineering Structures 198 (2019) 109473. `doi:10.1016/j.engstruct.2019.109473`.

44

[11] G. Kouroussis, H. P. Mouzakis, K. E. Vogiatzis, Structural impact response for assessing railway vibration induced on buildings, Mechanics & Industry 18 (8) (2017) 803. `doi:10.1051/meca/2017043`.

[12] Y. E. Ibrahim, M. Nabil, Finite element analysis of multistory structures subjected to train-induced vibrations considering soil-structure interaction, Case Studies in Construction Materials (2021) e00592`doi:10.1016/j.cscm.2021.e00592`.

[13] P. Amado-Mendes, P. A. Costa, L. M. Godinho, P. Lopes, 2.5 D MFS–FEM model for the prediction of vibrations due to underground railway traffic, Engineering Structures 104 (2015) 141–154. `doi:10.1016/j.engstruct.2015.09.013`.

[14] C. Zou, Y. Wang, Z. Tao, Train-induced building vibration and radiated noise by considering soil properties, Sustainability 12 (3) (2020) 937. `doi:10.3390/su12030937`.

[15] A. Cicirello, R. S. Langley, Efficient parametric uncertainty analysis within the hybrid finite element/statistical energy analysis method, Journal of Sound and Vibration 333 (6) (2014) 1698–1717. `doi:10.1016/j.jsv.2013.10.040`.

[16] S. Eftekhar Azam, E. Chatzi, C. Papadimitriou, A dual kalman filter approach for state estimation via output-only acceleration measurements, Mechanical Systems and Signal Processing 60-61 (2015) 866–886. `doi:10.1016/j.ymssp.2015.02.001`.

[17] K. Maes, G. De Roeck, A. Iliopoulos, W. Weijtjens, C. Devriendt, G. Lombaert, Kalman filter based strain estimation for fatigue assessment of an offshore monopile wind turbine, Proceeding of ISMA2016 including USD2016 (2016).

[18] M. Henkel, N. Noppe, W. Weijtjens, C. Devriendt, Subsoil stress reconstruction for fatigue monitoring of offshore wind turbine using accelerometers on the tower, in: European Workshop on Structural Health Monitoring, Vol. 11, ndt.net, 2018, pp. 1 – 12.

[19] A. Iliopoulos, W. Weijtjens, D. Van Hemelrijck, C. Devriendt, Fatigue assessment of offshore wind turbines on monopile foundations using multi-band modal expansion, Wind Energy 20 (8) (2017) 1463–1479. `doi:10.1002/we.2104`.

[20] J. Kullaa, Bayesian virtual sensing in structural dynamics, Mechanical Systems and Signal Processing 115 (2019) 497–513. `doi:10.1016/j.ymssp.2018.06.010`.

[21] B. Hofmeister, M. Bruns, R. Rolfes, Finite element model updating using deterministic optimisation: A global pattern search approach, Engineering Structures 195 (2019) 373–381. `doi:10.1016/j.engstruct.2019.05.047`.

[22] M. Sanayei, C. R. Brett, J. A. Zapfe, E. E. Ungar, E. M. Hines, Predicting train-induced vibrations in multi-story buildings, in: Structures Congress 2008: Crossing Borders, 2008, pp. 1–10.

[23] M. Sanayei, A. Kayiparambil P., J. A. Moore, C. R. Brett, Measurement and prediction of train-induced vibrations in a full-scale building, Engineering Structures 77 (2014) 119 – 128. `doi:10.1016/j.engstruct.2014.07.033`.

[24] C. Zou, J. A. Moore, M. Sanayei, Y. Wang, Impedance model for estimating train-induced building vibrations, Engineering Structures 172 (2018) 739–750.

[25] L. Auersch, Simple and fast prediction of train-induced track forces, ground and building vibrations, Railway Engineering Science 28 (3) (2020) 232–250.

[26] W. Weijtjens, G. D. Sitter, C. Devriendt, P. Guillaume, Operational modal parameter estimation of mimo systems using transmissibility functions, Automatica 50 (2) (2014) 559 – 564. `doi:10.1016/j.automatica.2013.11.021`.

[27] R. J. Allemang, D. L. Brown, Experimental modal analysis and dynamic component synthesis. volume 1. summary of technical work, Tech. rep., University of Cincinnati, Structural Dynamics Research Laboratory (1987).

[28] N. Maia, J. Silva, A. Ribeiro, The transmissibility concept in multi-degree-of-freedom systems, Mechanical Systems and Signal Processing 15 (1) (2001) 129 – 137. `doi:10.1006/mssp.2000.1356`.

[29] M. Tarpø, B. Nabuco, C. Georgakis, R. Brincker, Expansion of experimental mode shape from operational modal analysis and virtual sensing for fatigue analysis using the modal expansion method, International Journal of Fatigue 130 (2020) 105280. `doi:10.1016/j.ijfatigue.2019.105280`.

[30] B. Peeters, System identification and damage detection in civil engineering, Dissertation, Katholieke Universiteit Leuven (2000).

[31] C. D. Petersen, R. Fraanje, B. S. Cazzolato, A. C. Zander, C. H. Hansen, A kalman filter approach to virtual sensing for active noise control, Mechanical Systems and Signal Processing 22 (2) (2008) 490–508. `doi:10.1016/j.ymssp.2007.06.007`.

[32] P. van Overschee, B. de Moor, Subspace Identification for Linear Systems: Theory — Implementation — Applications, Springer US, 2012.

[33] D. Simon, Optimal State Estimation: Kalman, H-Infinity, and Nonlinear Approaches, Wiley-Interscience, 2006.

[34] C. Rainieri, G. Fabbrocino, Operational modal analysis of civil engineering structures, Springer, 2014.

[35] R. E. Powell, W. Seering, Multichannel Structural Inverse Filtering, Journal of Vibration, Acoustics, Stress, and Reliability in Design 106 (1) (1984) 22–28. `doi:10.1115/1.3269147`.

[36] T. Chen, H. Ohlsson, L. Ljung, On the estimation of transfer functions, regularizations and gaussian processes—revisited, Automatica 48 (8) (2012) 1525–1535. `doi:https://doi.org/10.1016/j.automatica.2012.05.026`.

[37] L. Ljung, System identification toolbox reference, Reference, The MathWorks, Inc, Natick, MA (2017).

[38] J. O. Smith, Introduction to digital filters: with audio applications, Vol. 2, Julius Smith, 2007.

[39] W. H. Kwon, P. S. Kim, S. H. Han, A receding horizon unbiased fir filter for discrete-time state space models, Automatica 38 (3) (2002) 545–551. `doi:10.1016/S0005-1098(01)00242-4`.

[40] P.-S. Kim, An alternative fir filter for state estimation in discrete-time systems, Digital Signal Processing 20 (3) (2010) 935–943. `doi:10.1016/j.dsp.2009.10.033`.

[41] A. Cetin, O. Gerek, Y. Yardimci, Equiripple fir filter design by the fft algorithm, IEEE Signal Processing Magazine 14 (2) (1997) 60–64. `doi:10.1109/79.581378`.

[42] T. N. Davidson, Enriching the art of fir filter design via convex optimization, IEEE Signal Processing Magazine 27 (3) (2010) 89–101. `doi:10.1109/MSP.2010.936040`.

[43] J. G. Proakis, Digital signal processing: principles algorithms and applications, Pearson Education India, 2001.

[44] M. Paz, Y. H. Kim, Structural dynamics, Springer, 2019.

[45] R. L. Williams, D. A. Lawrence, et al., Linear state-space control systems, John Wiley & Sons, 2007.

[46] K. Ozeki, T. Umeda, An adaptive filtering algorithm using an orthogonal projection to an affine subspace and its properties, Electronics and Communications in Japan (Part I: Communications) 67 (5) (1984) 19–27. `doi:10.1002/ecja.4400670503`.

[47] A. N. Tikhonov, A. S. Leonov, A. G. Yagola, Nonlinear ill-posed problems, Springer Netherlands, 1998.

[48] P. S. Diniz, Adaptive filtering, Springer, 1997.

[49] A. Jiang, H. K. Kwan, Y. Zhu, X. Liu, N. Xu, X. Yao, Peak-error-constrained sparse FIR filter design using iterative L1 optimization, in: 2016 24th European Signal Processing Conference (EUSIPCO), 2016, pp. 180–184. `doi:10.1109/EUSIPCO.2016.7760234`.

[50] Y. Neuvo, Dong Cheng-Yu, S. Mitra, Interpolated finite impulse response filters, IEEE Transactions on Acoustics, Speech, and Signal Processing 32 (3) (1984) 563–570. `doi:10.1109/TASSP.1984.1164348`.

[51] C.-S. Wu, A.-Y. Wu, A novel cost-effective multi-path adaptive interpolated FIR (IFIR)-based echo canceller, in: 2002 IEEE International Symposium on Circuits and Systems. Proceedings (Cat. No. 02CH37353), Vol. 5, IEEE, 2002, pp. V–V. `doi:10.1109/ISCAS.2002.1010738`.

[52] A. Mehrnia, A. N. Willson, On optimal IFIR filter design, in: 2004 IEEE International Symposium on Circuits and Systems (IEEE Cat. No.04CH37512), Vol. 3, 2004, pp. III–133. `doi:10.1109/ISCAS.2004.1328701`.

[53] T. K. Roy, M. Morshed, Performance analysis of low pass FIR filters design using Kaiser, Gaussian and Tukey window function methods, in: 2013 2nd International Conference on Advances in Electrical Engineering (ICAEE), 2013, pp. 1–6. `doi:10.1109/ICAEE.2013.6750294`.

[54] L. Ljung, System Identification – Theory for the User, Prentice Hall, 1998.

[55] P. Stoica, Y. Selen, Model-order selection: a review of information criterion rules, IEEE Signal Processing Magazine 21 (4) (2004) 36–47. `doi:10.1109/MSP.2004.1311138`.

[56] C. Fenu, L. Reichel, G. Rodriguez, H. Sadok, GCV for Tikhonov regularization by partial SVD, BIT Numerical Mathematics 57 (4) (2017) 1019–1039. `doi:10.1007/s10543-017-0662-0`.

[57] K. Koziol, Designing of buildings in the aspect of prediction of people from traffic included vibrations, IOP Conference Series: Materials Science and Engineering 603 (2019) 042072. `doi:10.1088/1757-899x/603/4/042072`.

[58] A. Gidlöf-Gunnarsson, M. Ögren, T. Jerson, E. Öhrström, et al., Railway noise annoyance and the importance of number of trains, ground vibration, and building situational factors, Noise and Health 14 (59) (2012) 190.

[59] G. Kerschen, K. Worden, A. F. Vakakis, J.-C. Golinval, Past, present and future of nonlinear system identification in structural dynamics, Mechanical Systems and Signal Processing 20 (3) (2006) 505 – 592. `doi:10.1016/j.ymssp.2005.04.008`.

[60] M. Lou, H. Wang, X. Chen, Y. Zhai, Structure-soil-structure interaction: Literature review, Soil Dynamics and Earthquake Engineering 31 (12) (2011) 1724 – 1731. `doi:10.1016/j.soildyn.2011.07.008`.

[61] B. Hofmeister, C. Jonscher, C. Hübler, R. Rolfes, Damage localisation by residual energy from multiple-input finite impulse response prognosis, in: European Workshop on Structural Health Monitoring, Springer International Publishing, 2021, pp. 711–719.